

1  
2  
3  
4  
5  
6  
7  
8  
9  
10  
11  
12  
13  
14  
15  
16  
17  
18  
19  
20  
21  
22  
23  
24  
25  
26  
27  
28  
29  
30  
31  
32  
33  
34  
35  
36  
37  
38  
39  
40  
41  
42  
43  
44  
45  
46

## **Rapalogs downmodulate intrinsic immunity and promote cell entry of SARS-CoV-2**

Guoli Shi<sup>1</sup>, Abhilash I. Chiramel<sup>2</sup>, Saliha Majdoul<sup>1</sup>, Kin Kui Lai<sup>1</sup>, Tirhas Dempsey<sup>1</sup>, Adam Kenney<sup>3</sup>, Ashley Zani<sup>3</sup>, Adrian Eddy<sup>3</sup>, Lizhi Zhang<sup>3</sup>, Paul A. Beare<sup>4</sup>, Swagata Kar<sup>5</sup>, Jacob S. Yount<sup>3</sup>, Sonja M. Best<sup>4</sup>, Alex A. Compton<sup>1,\*</sup>

<sup>1</sup>HIV Dynamics and Replication Program, Center for Cancer Research, National Cancer Institute, Frederick, MD, USA

<sup>2</sup>Laboratory of Virology, Rocky Mountain Laboratories, National Institute of Allergy and Infectious Diseases, Hamilton, MT, USA

<sup>3</sup>Department of Microbial Infection and Immunity, The Ohio State University, Columbus, OH, USA

<sup>4</sup>Laboratory of Bacteriology, Rocky Mountain Laboratories, National Institute of Allergy and Infectious Diseases, Hamilton, MT, USA

<sup>5</sup>Bioqual, Rockville, MD, USA

\* Address correspondence to [alex.compton@nih.gov](mailto:alex.compton@nih.gov)

Running title: Rapalogs promote cell entry of SARS-CoV-2

Keywords: rapamycin, rapalog, mTOR inhibitor, IFITM, interferon, SARS-CoV-2, TFEB, microautophagy, COVID-19, coronavirus, membrane fusion

## 47 **Abstract**

48  
49 SARS-CoV-2 infection in immunocompromised individuals is associated with prolonged virus  
50 shedding and the evolution of viral variants. Rapamycin and its analogs (rapalogs, including  
51 everolimus, temsirolimus, and ridaforolimus) are FDA-approved as mTOR inhibitors in clinical  
52 settings such as cancer and autoimmunity. Rapalog use is commonly associated with increased  
53 susceptibility to infection, which has been traditionally explained by impaired adaptive  
54 immunity. Here, we show that exposure to rapalogs increases susceptibility to SARS-CoV-2  
55 infection in tissue culture and in immunologically naïve rodents by antagonizing the cell-intrinsic  
56 immune response. By identifying one rapalog (ridaforolimus) that is less active in this regard, we  
57 demonstrate that rapalogs promote Spike-mediated entry into cells by triggering the degradation  
58 of IFITM2 and IFITM3 via an endolysosomal remodeling program known as microautophagy.  
59 Rapalogs that promote virus entry inhibit the mTOR-mediated phosphorylation of the  
60 transcription factor TFEB, which facilitates its nuclear translocation and triggers  
61 microautophagy. In rodent models of infection, injection of rapamycin prior to and after virus  
62 exposure resulted in elevated SARS-CoV-2 replication and exacerbated viral disease, while  
63 ridaforolimus had milder effects. Overall, our findings indicate that preexisting use of certain  
64 rapalogs may elevate host susceptibility to SARS-CoV-2 infection and disease by activating a  
65 lysosome-mediated suppression of intrinsic immunity.

## 66 67 **Significance**

68  
69 Rapamycin is an immunosuppressant used in humans to treat cancer, autoimmunity, and other  
70 disease states. Here, we show that rapamycin and related compounds promote the first step of the  
71 SARS-CoV-2 infection cycle—entry into cells—by disarming cell-intrinsic immune defenses.  
72 We outline the molecular basis for this effect by identifying a rapamycin derivative that is  
73 inactive, laying the foundation for improved mTOR inhibitors that do not suppress intrinsic  
74 immunity. We find that rapamycin analogs that promote SARS-CoV-2 entry are those that  
75 activate TFEB, a transcription factor that triggers the degradation of antiviral membrane proteins  
76 inside of cells. Finally, rapamycin administration to rodents prior to SARS-CoV-2 challenge  
77 results in enhanced viral disease, revealing that its use in humans may increase susceptibility to  
78 infection.

## 79 80 **Introduction**

81  
82 Severe acute respiratory syndrome (SARS) coronavirus (CoV)-2 emerged in humans in  
83 2019 following a species jump from bats and a possible intermediate animal host and is the cause  
84 of COVID-19, a respiratory and multi-organ disease of variable severity [1, 2]. The  
85 characterization of virus-host interactions that dictate SARS-CoV-2 infection and COVID-19  
86 severity is a major priority for public health [3]. Immune impairment, such as that resulting from  
87 cancer, has been associated with prolonged SARS-CoV-2 shedding and the seeding of “super-  
88 spreader” events [4-8].

89 One group of compounds being considered for the treatment of COVID-19-related  
90 immunopathology are rapamycin (sirolimus, Rapamune) and rapamycin analogs (rapalogs) [9-  
91 20]. As Food and Drug Administration-approved inhibitors of mammalian target of rapamycin  
92 (mTOR) kinase, these macrolide compounds are used therapeutically to inhibit the processes of

93 cancer, autoimmunity, graft versus host disease, atherosclerosis, and aging [21]. Rapalogs,  
94 including everolimus (RAD-001), temsirolimus (Torisel, CCI-779), and ridaforolimus  
95 (deforolimus, AP-23573), were developed to decrease the half-life of rapamycin *in vivo* in order  
96 to minimize the systemic immunosuppression caused by rapamycin use, which is associated with  
97 increased susceptibility to infections [22-26]. Differing by only a single functional group at  
98 carbon-40 (**Figure 1**), it is believed that rapamycin and rapalogs share the same molecular  
99 mechanism of action to inhibit mTOR kinase—they bind to FK506-binding proteins (FKBP) and  
100 the resulting complex physically interacts with mTOR and disrupts its signaling [25, 27].

101 Activation of mTOR promotes cell growth, cell proliferation, and cell survival [28]. In  
102 addition, mTOR activation promotes pro-inflammatory T-cell differentiation and mTOR  
103 inhibitors have been used to block lymphocyte proliferation and cytokine storm [29]. Since  
104 respiratory virus infections like SARS-CoV-2 can cause disease by provoking hyper-  
105 inflammatory immune responses that result in immunopathology [30-32], rapalogs are being  
106 tested as treatments to decrease viral disease burden. At least three active clinical trials have been  
107 designed to test the impact of rapamycin on COVID-19 severity in infected patients  
108 (NCT04461340, NCT04341675, NCT04371640).

109 In addition to their potential utility for mitigating disease in individuals already infected  
110 by SARS-CoV-2, there are also calls to use rapalogs as antiviral agents to inhibit virus infection  
111 itself (i.e. as a prophylactic) [33]. It was recently shown that rapalogs inhibit SARS-CoV-2  
112 replication when added to cells post-infection [34], attesting to a potential use of rapalogs as  
113 antivirals in infected individuals. Nonetheless, rapalogs are known to induce an  
114 immunosuppressed state in humans characterized by an increased rate of infections, including  
115 those caused by respiratory viruses. Furthermore, rapamycin administration concurrent with  
116 virus challenge has been shown to promote Influenza A replication in mice and to exacerbate  
117 viral disease [35, 36], but the mechanism was unknown. We previously found that exposure of  
118 human and murine cells to rapamycin induced the lysosomal degradation of a select group of  
119 cellular proteins, including the interferon-inducible transmembrane (IFITM) proteins, and  
120 rendered cells more permissive to infection by Influenza A virus and gene-delivering lentiviral  
121 vectors [37, 38]. IFITM1, IFITM2, and IFITM3 are expressed constitutively in a variety of  
122 tissues, are further upregulated by type-I and type-II interferons, and are important components  
123 of cell-intrinsic immunity, the antiviral network that defends individual cells against virus  
124 invasion [39, 40]. Nonetheless, it remained to be determined how rapamycin-mediated regulation  
125 of intrinsic immunity impacts host susceptibility to virus infection *in vivo*.

126 In this report, we show that rapalogs differentially counteract the constitutive and  
127 interferon-induced antiviral state in lung cells and increase permissiveness to SARS-CoV-2  
128 infection. We found that the enhancing effect of rapalogs on SARS-CoV-2 infection is  
129 functionally linked to their capacity to trigger degradation of IFITM proteins, particularly  
130 IFITM2 and IFITM3. By identifying a rapalog that lacks this activity, we found that IFITM  
131 protein turnover and SARS-CoV-2 infection enhancement are associated with activation of  
132 TFEB, a master regulator of lysosome function that is regulated by mTOR. Administration of  
133 rapamycin to naive rodents four hours prior to experimental SARS-CoV-2 infection increased  
134 virus replication and viral disease severity, indicating for the first time that suppression of  
135 intrinsic immunity by rapamycin contributes to its immunosuppressive properties *in vivo*.

136  
137 **Results**

138

139 **Select rapalogs promote SARS-CoV-2 infection and downmodulate IFITM proteins in lung**  
140 **cells**

141

142 To assess how rapamycin and rapalogs impact SARS-CoV-2 infection, we took  
143 advantage of a pseudovirus system based on human immunodeficiency virus (HIV). This  
144 pseudovirus (HIV-CoV-2 S) is limited to a single round of infection, cell entry is mediated by  
145 SARS-CoV-2 Spike, and infection of target cells is measured by luciferase activity. SARS-CoV-  
146 2 can enter cells via multiple routes, and sequential proteolytic processing of Spike is essential to  
147 this process. SARS-CoV-2 Spike is cleaved at a polybasic motif (RRAR) located at the S1/S2  
148 boundary by furin-like proteases in virus-producing cells prior to release. Subsequently, the S2'  
149 site is cleaved by the trypsin-like proteases TMPRSS2 on the target cell surface or cathepsins B  
150 and L in target cell endosomes, triggering membrane fusion at those sites [41-43].

151 We previously found that a four-hour pre-treatment of cells with 20  $\mu$ M quantities of  
152 rapamycin triggered the degradation of human IFITM3 and enhanced cellular susceptibility to  
153 Influenza A infection [44]. Therefore, we pre-treated A549-ACE2 (transformed human lung  
154 epithelial cells that overexpress the human ACE2 receptor) with 20  $\mu$ M rapamycin, everolimus,  
155 temsirolimus, ridaforolimus, or DMSO (vehicle control) for four hours and then challenged cells  
156 with HIV-CoV-2. Interestingly, we found that rapalogs promoted Spike-mediated infection to  
157 different extents: rapamycin, everolimus, and temsirolimus significantly enhanced infection (up  
158 to 5-fold) while ridaforolimus did not (**Figure 2A**). To determine whether rapalogs promote cell  
159 permissiveness to infection by upregulating dependency factors or by downregulating restriction  
160 factors, we performed the same experiment in cells pre-treated with type-I interferon. While  
161 type-I interferon suppressed infection by approximately 90%, the addition of rapamycin,  
162 everolimus, and temsirolimus resulted in rescue of infection by up to 20-fold (**Figure 2A**). As a  
163 result, infection levels were partially restored to those achieved in the absence of interferon, with  
164 everolimus having the greatest boosting effect and ridaforolimus, the least. Therefore, rapalogs  
165 differentially promote SARS-CoV-2 Spike-mediated infection by counteracting intrinsic antiviral  
166 defenses in lung cells to different extents.

167 Type-I interferon treatment of A549-ACE2 resulted in upregulation of *IFITM2* and  
168 *IFITM3*, as detected by an antibody recognizing both proteins in whole cell lysates (**Figure 2B**).  
169 A549-ACE2 cells express low but detectable levels of IFITM2/3 in the absence of interferon  
170 treatment (**Supplemental Figure 1A**). Consistent with our previous publication, addition of  
171 rapamycin resulted in substantial loss of IFITM2/3 protein levels from cells. In a manner that  
172 mirrored the differential effects of rapalogs on pseudovirus infection, everolimus and  
173 temsirolimus greatly diminished IFITM2/3 levels while ridaforolimus reduced IFITM2/3 to a  
174 lesser extent (**Figure 2B and Supplemental Figure 1A**). In contrast, ACE2 levels were not  
175 affected by interferon nor by rapalog treatment. Therefore, rapamycin derivatives may facilitate  
176 infection by antagonizing constituents of intrinsic immunity, including IFITM2/3, and this  
177 activity is determined by the chemical moiety found at carbon-40 of the macrolide structure.

178 To extend our findings to primary lung cells, we performed similar experiments in human  
179 small airway epithelial cells (HSAEC). While these cells were not permissive to HIV-CoV-2,  
180 they were susceptible to infection by pseudovirus based on vesicular stomatitis virus (VSV-CoV-  
181 2) whereby infection is reported by GFP expression. Pre-treatment of HSAEC with rapalogs  
182 enhanced VSV-CoV-2 infection to varying extents, but as observed in A549-ACE2 cells,  
183 everolimus exhibited the greatest effect and ridaforolimus, the least. Endogenous IFITM3 was  
184 readily detected in HSAEC under basal conditions (in the absence of interferon), while IFITM1

185 was barely detected and IFITM2 was not detected at all, and IFITM3 levels were  
186 downmodulated differentially by rapalogs (**Supplemental Figure 1B**). siRNA-mediated  
187 knockdown of IFITM3 in HSAEC resulted in enhanced VSV-CoV-2 infection, indicating that  
188 IFITM3 restricts Spike-mediated infection in these cells (**Supplemental Figure 1C**). We also  
189 treated semi-transformed nasal epithelial cells known as UNC223A with rapalogs in order to  
190 assess an impact on endogenous IFITM3 levels. As observed in HSAEC, downmodulation of  
191 IFITM3 occurred following treatment of UNC223A with rapamycin, everolimus,  
192 temsirolimus, and to a lesser extent, ridaforolimus (**Supplemental Figure 1D**).

193 Since 20  $\mu$ M quantities of rapalogs promoted pseudovirus infection mediated by SARS-  
194 CoV-2 Spike, we tested how pretreatment of A549-ACE2 cells with varying amounts of  
195 everolimus impacted infection by replication-competent SARS-CoV-2. We observed a dose-  
196 dependent enhancement of infectious SARS-CoV-2 yield in supernatants of infected cells (up to  
197 4-fold) (**Figure 2D**). Therefore, everolimus boosts pseudovirus infection and SARS-CoV-2  
198 infection to similar extents, and since Spike is the only viral component shared between the two  
199 sources of infection, cellular entry is the infection stage inhibited by the intrinsic defenses that  
200 are sensitive to downmodulation by rapalogs.

201

### 202 **Rapalogs facilitate cell entry mediated by various viral fusion proteins**

203

204 In order to gain a greater mechanistic understanding of the effects of rapalogs on SARS-  
205 CoV-2 infection, we took advantage of HeLa cells overexpressing ACE2 (HeLa-ACE2). HeLa-  
206 ACE2 were pre-treated for four hours with increasing amounts of everolimus and then  
207 challenged with SARS-CoV-2. Everolimus increased titers of infectious virus released into  
208 supernatants in a dose-dependent manner, and to a greater extent than was observed for A549-  
209 ACE2 cells (**Figure 3A**). Furthermore, we found that pre-treatment of cells with 20  $\mu$ M amounts  
210 of rapalogs enhanced SARS-CoV-2 titers to varying extents—rapamycin, everolimus, and  
211 temsirolimus significantly boosted SARS-CoV-2 infection (up to 10-fold), while ridaforolimus  
212 had less of an impact (**Figure 3B**). We also performed infections of HeLa-ACE2 with HIV-CoV-  
213 2 pseudovirus, and the results were similar: the impact of ridaforolimus was minimal while the  
214 other three compounds significantly boosted Spike-mediated infection (**Figure 3C**). To test the  
215 link between infection enhancement and downmodulation of IFITM proteins by rapalogs, we  
216 probed for levels of IFITM3, IFITM2, and IFITM1 by immunoblotting whole cell lysates using  
217 specific antibodies. All IFITM proteins were readily detected in HeLa-ACE2 in the absence of  
218 interferon. IFITM3, IFITM2, and IFITM1 were significantly downmodulated following  
219 treatment with rapamycin, everolimus, and temsirolimus (**Figure 3D**). Levels of IFITM3 were  
220 quantified over multiple experiments and presented as an average. The results show that all  
221 rapalogs led to significant decreases in IFITM3 protein, but ridaforolimus was least potent in this  
222 regard (**Figure 3E**). The loss of IFITM2/3 protein was confirmed by confocal  
223 immunofluorescence microscopy of intact cells (**Figure 3F**). Furthermore, prolonged treatment  
224 (24 hours) of cells with everolimus and temsirolimus resulted in prolonged suppression of  
225 IFITM2 and IFITM3 protein levels (**Supplemental Figure 2A**). In contrast, ACE2 levels and  
226 ACE2 subcellular distribution were unaffected by rapalog treatment (**Figure 3D and**  
227 **Supplemental Figure 2B**). Furthermore, rapalogs did not significantly decrease cell viability  
228 under the conditions tested (**Supplemental Figure 2C**).

229 We previously showed that lysosomal degradation of IFITM3 triggered by rapamycin  
230 requires endosomal complexes required for transport (ESCRT) machinery and multivesicular

231 body (MVB)-lysosome fusion [44]. We confirmed that depletion of IFITM proteins by rapalogs  
232 occurs at the post-translational level and requires endolysosomal acidification, since bafilomycin  
233 A1 prevented their loss (**Supplemental Figure 3A-B**). The process by which rapalogs trigger  
234 IFITM protein degradation resembles endolysosomal microautophagy, an autophagy pathway  
235 that does not require an autophagosome intermediate [45-47]. Treatment of cells with U18666A,  
236 an inhibitor of MVB formation and microautophagy, mostly prevented IFITM3 turnover in the  
237 presence of rapalogs (**Supplementary Figure 3B**). In contrast, a selective inhibitor of  
238 vps34/PI3KC3 (essential for macroautophagy induction) did not (**Supplemental Figure 3C-D**).  
239 Therefore, rapamycin and specific rapalogs trigger the degradation of endogenous factors  
240 mediating intrinsic resistance to SARS-CoV-2 infection, including the IFITM proteins, by  
241 promoting their turnover in lysosomes via endolysosomal microautophagy.

242 Enveloped virus entry into cells is a concerted process involving virus attachment to the  
243 cell surface followed by fusion of cellular and viral membranes. Since IFITM proteins are known  
244 to inhibit virus-cell membrane fusion, we quantified the terminal stage of HIV-CoV-2 entry by  
245 tracking the cytosolic delivery of beta-lactamase (Blam) in single cells. We found that treatment  
246 of cells with rapamycin, everolimus, and temsirolimus resulted in enhanced HIV-CoV-2 entry  
247 while ridaforolimus was less impactful (**Figure 4A**). To measure whether rapalogs promote the  
248 cell entry process driven by other coronavirus Spike proteins, we produced HIV incorporating  
249 Spike from SARS-CoV (HIV-CoV-1) or MERS-CoV (HIV-MERS-CoV). Infections by both  
250 HIV-CoV-1 and HIV-MERS-CoV were elevated by rapalog treatment in HeLa-ACE2 and HeLa-  
251 DPP4 cells, respectively, although the extent of enhancement was lower than that observed with  
252 HIV-CoV-2 (**Figure 4B-C**). Consistently, ridaforolimus was the least active among the rapalogs  
253 tested and it did not significantly promote pseudovirus infection. Since we previously showed  
254 that rapamycin enhanced the cellular entry of Influenza A virus and VSV-G pseudotyped  
255 lentiviral vectors [44], we also assessed infection of pseudoviruses incorporating hemagglutinin  
256 (HIV-HA) or VSV G (HIV-VSV G). Rapamycin, everolimus, and especially temsirolimus  
257 boosted HA- and VSV G-mediated infections (up to 30-fold and 11-fold, respectively) (**Figure**  
258 **4D-E**). Since IFITM proteins have been previously shown to inhibit infection by SARS-CoV-1,  
259 MERS-CoV, VSV, and Influenza A virus [40], these data suggest that rapalogs promote  
260 infection, at least in part, by lowering the barrier to virus entry imposed by IFITM proteins.

### 261 262 **IFITM2/3 mediate the rapalog-sensitive barrier to SARS-CoV-2 infection in HeLa-ACE2**

263  
264 To formally test the link between rapalog-mediated depletion of IFITM proteins and  
265 entry by SARS-CoV-2 Spike, we used HeLa cells in which IFITM1, IFITM2, and IFITM3 were  
266 knocked out (*IFITM1-3* KO) and introduced human ACE2 by transient transfection (**Figure 5A**).  
267 IFITM2 alone or IFITM2 and IFITM3 were restored in *IFITM1-3* KO cells by transient  
268 overexpression (**Figure 5B**) and cells were challenged with HIV-CoV-2. Relative to WT cells,  
269 HIV-CoV-2 infection was approximately 50-fold higher in *IFITM1-3* KO cells, indicating that  
270 endogenous IFITM proteins restrict SARS-CoV-2 Spike-mediated infection in this cell type.  
271 Furthermore, while temsirolimus significantly promoted infection by 10-fold in WT cells, little  
272 to no enhancement was observed in *IFITM1-3* KO cells (**Figure 5C**). Ectopic expression of  
273 IFITM2 inhibited infection and partially restored sensitivity to temsirolimus, while the  
274 combination of IFITM2 and IFITM3 restricted infection further and fully restored temsirolimus  
275 sensitivity. These findings indicate that temsirolimus promotes Spike-mediated infection in  
276 HeLa-ACE2 cells by lowering levels of endogenous IFITM2 and IFITM3.

277 Since human IFITM proteins have been reported to promote SARS-CoV-2 infection in  
278 certain cell types, including the lung epithelial cell line Calu-3 [48], we tested the impact of  
279 rapalogs on HIV-CoV-2 infection in this cell type. Here, in contrast to the enhancement observed  
280 in A549-ACE2 and HeLa-ACE2 cells, rapamycin, everolimus, and temsirolimus inhibited Spike-  
281 mediated infection in Calu-3 cells (**Supplemental Figure 4**). These results confirm that the  
282 effect of rapalog treatment on Spike-mediated infection is explained by their ability to induce the  
283 degradation of IFITM proteins.

284

### 285 **Rapalogs differentially activate a lysosomal degradation pathway orchestrated by TFEB**

286

287 Since rapamycin and rapalogs are known to inhibit mTOR signaling by binding both  
288 mTOR and FKBP12 (and other FKBP members), we sought to determine whether mTOR  
289 binding and its inhibition are required for rapalog-mediated enhancement of SARS-CoV-2  
290 infection. To that end, we tested the effect of tacrolimus (also known as FK506), a macrolide  
291 immunosuppressant that is chemically related to rapalogs but does not bind nor inhibit mTOR.  
292 Instead, tacrolimus forms a ternary complex with FKBP12 and calcineurin to inhibit the  
293 signaling properties of the latter [49]. In HeLa-ACE2 cells, a four-hour treatment of 20  $\mu$ M  
294 tacrolimus did not reduce levels of IFITM2/3 (**Supplemental Figure 5A**), nor did it boost HIV-  
295 CoV-2 infection (**Supplemental Figure 5B**). These results suggest that FKBP12 binding is not  
296 sufficient for drug-mediated enhancement of SARS-CoV-2 infection. They also suggest that the  
297 extent to which mTOR is inhibited may explain the differential degree to which infection is  
298 impacted by the immunosuppressants examined in this study. Therefore, we surveyed the  
299 phosphorylation status of TFEB, a transcription factor that controls lysosome biogenesis and  
300 degradative processes carried out by lysosomes [50]. mTOR phosphorylates TFEB at serine 211  
301 (S211), which promotes its sequestration in the cell cytoplasm and decreases its translocation  
302 into the nucleus [50-52]. Furthermore, this phosphorylation event was previously shown to be  
303 sensitive to inhibition by rapamycin and temsirolimus [51, 53]. We found that rapamycin,  
304 everolimus, and temsirolimus significantly reduced S211 phosphorylation of endogenous TFEB  
305 in A549-ACE2 cells while ridaforolimus did so to a lesser extent (**Figure 6A-B**). Furthermore,  
306 we measured the subcellular distribution of TFEB-GFP in HeLa-ACE2 treated with different  
307 compounds and found that rapamycin, everolimus, and temsirolimus induced a significantly  
308 greater accumulation of TFEB-GFP in the nucleus (**Figure 6C-D**). These findings suggest that  
309 ridaforolimus exhibits a less potent inhibition of mTOR-mediated TFEB phosphorylation under  
310 the conditions tested. Therefore, nuclear translocation of TFEB is associated with IFITM2/3  
311 degradation and increased cellular susceptibility to SARS-CoV-2 Spike-mediated infection.  
312 Consistent with a direct relationship between TFEB activation, IFITM2/3 turnover, and Spike-  
313 mediated cell entry, we found that ectopic expression of a constitutively active form of TFEB  
314 lacking the first 30 amino-terminal residues [50] was sufficient to trigger IFITM2/3 loss from  
315 cells (**Figure 6E**) and sufficient to increase susceptibility to HIV-CoV-2 infection (**Figure 6F**).  
316 By combining transfection of the constitutively active form of TFEB with temsirolimus  
317 treatment, we found that IFITM2/3 levels were strongly suppressed irrespective of whether  
318 TFEB was detected or not. This confirms that TFEB and rapalogs are functionally redundant and  
319 operate in the same pathway to negatively regulate IFITM2/3 levels (**Supplemental Figure 5C**).  
320 Finally, we took advantage of TFEB-deficient cells to formally address the role that TFEB  
321 activation plays during rapalog-mediated enhancement of infection (**Supplemental Figure 5D**).  
322 While rapamycin, everolimus, and temsirolimus significantly boosted HIV-CoV-2 infection in

323 HeLa WT cells transfected with ACE2, no significant enhancement was observed in HeLa *TFEB*  
324 KO cells (**Figure 6G**). In summary, our results employing functionally divergent rapalogs reveal  
325 a previously unrecognized immunoregulatory role played by the mTOR-TFEB-lysosome axis  
326 that affects the cell entry of SARS-CoV-2 and other viruses.

### 327 328 **Rapamycin enhances SARS-CoV-2 infection and viral disease *in vivo***

329  
330 Our findings from SARS-CoV-2 and pseudovirus infection of human cells demonstrate  
331 that rapamycin, everolimus, and temsirolimus can suppress intrinsic immunity at the post-  
332 translational level, while ridaforolimus does so to a lesser extent. However, whether these  
333 compounds are functionally divergent when administered *in vivo* was unclear. Since  
334 temsirolimus is a prodrug of rapamycin (it is metabolized to rapamycin), and since rapamycin  
335 was previously shown to promote morbidity of Influenza A infection in mice [36, 54], we tested  
336 how intraperitoneal injection of rapamycin or ridaforolimus impacted SARS-CoV-2 replication  
337 and disease course in naïve hamsters (**Figure 7A**). Hamsters are a permissive model for SARS-  
338 CoV-2 because hamster ACE2 is sufficiently similar to human ACE2 to support productive  
339 infection. Furthermore, in contrast to transgenic mice expressing human ACE2 or mice infected  
340 with mouse-adapted (MA) SARS-CoV-2, hamsters exhibit severe disease characterized by lung  
341 pathology when high viral loads are achieved [55].

342 Eight hamsters were randomly allocated to each group (rapamycin, ridaforolimus, or  
343 DMSO) and all received an intraperitoneal injection (3 mg/kg) 4 hours prior to intranasal  
344 inoculation with SARS-CoV-2. Furthermore, half of the mice in each group received a second  
345 injection on day 2 post-infection. As an indicator of infection and viral disease, we tracked  
346 weight loss for 10 days, or less if the hamster met requirements for euthanasia (loss of 20% or  
347 more of its body weight). We observed that hamsters receiving two injections did not exhibit  
348 significantly different rates of weight loss compared to those receiving a single injection  
349 (**Supplemental Figure 6**). As a result, we consolidated hamsters into three groups of eight  
350 according to receipt of rapamycin, ridaforolimus, or DMSO. Relative to DMSO treatment,  
351 hamsters injected with rapamycin or ridaforolimus exhibited significantly greater weight loss at  
352 days 2-5 post-infection, with rapamycin-treated hamsters displaying the most weight loss  
353 (**Figure 7B**). While one (1/8) of the hamsters treated with DMSO exhibited severe weight loss  
354 necessitating euthanasia, seven (7/8) of the hamsters treated with rapamycin were euthanized  
355 following severe weight loss between days 6 and 8 post-infection (**Figure 7C**). Meanwhile, four  
356 (4/8) of the hamsters treated with ridaforolimus met requirements for euthanasia on days 7 or 8  
357 post-infection. As a result, hamsters treated with rapamycin exhibited significantly reduced  
358 survival compared to the DMSO group (**Figure 7C**). In contrast, survival of ridaforolimus-  
359 treated animals did not differ significantly.

360 Survivors in all three groups recovered weight after day 7 post-infection and infectious  
361 virus was not detected from the lungs of these hamsters at day 10. In contrast, the lungs of  
362 hamsters euthanized due to severe weight loss exhibited high infectious virus titers, suggesting  
363 that morbidity was caused by viral pathogenesis (the lungs of one hamster treated with  
364 rapamycin were not examined because it was found dead following infection) (**Figure 7D**). To  
365 better understand the basis for differential survival between the groups, early SARS-CoV-2  
366 replication was measured by quantitative PCR from oral swabs. We found that hamsters injected  
367 with rapamycin exhibited significantly higher viral RNA levels in the oral cavity at day 2 post-  
368 infection compared to animals injected with DMSO (**Figure 7E**). In contrast, viral RNA levels in



369 hamsters injected with ridaforolimus were elevated relative to the DMSO group, but they did not  
370 differ significantly. Overall, these results suggest that rapamycin administration increases host  
371 susceptibility to SARS-CoV-2 infection and significantly increases morbidity and mortality.

372 We previously found that, like its human counterpart, murine IFITM3 is sensitive to  
373 depletion by rapamycin [44]. To determine whether rapamycin promotes host susceptibility to  
374 SARS-CoV-2 infection in mice, we injected C57BL/6 mice with rapamycin or DMSO prior to  
375 and after challenge with MA SARS-CoV-2 and measured infectious viral burden in lungs on day  
376 2 post-infection (**Figure 8A**). We found that virus titers in lungs were significantly increased  
377 (144-fold) in rapamycin-treated mice compared to DMSO-treated mice (**Figure 8B**).  
378 Furthermore, murine IFITM3 protein levels were reduced in the lungs of mice injected with  
379 rapamycin relative to levels found in DMSO-treated mice (**Figure 8C**). Together, these findings  
380 support the notion that rapamycin downmodulates intrinsic barriers to infection *in vivo*.

381

## 382 Discussion

383

384 By assessing their impact on infection at the single-cell and whole-organism level, we  
385 draw attention to an immunosuppressive property of rapamycin and some rapalogs that acts on  
386 cell-intrinsic immunity and increases cellular susceptibility to infection by SARS-CoV-2 and  
387 likely other pathogenic viruses. Side effects of rapalog use in humans, including increased risk of  
388 respiratory tract infections, are regularly attributed to immunosuppression of adaptive immunity  
389 [56]. Indeed, rapalogs have been used to mitigate systemic immunopathology caused by T-cell  
390 responses, and this is one reason why they are being tested for therapeutic benefit in COVID-19  
391 patients. However, since rapamycin was injected into immunologically naïve hosts prior to and  
392 soon after virus challenge, it is unlikely that rapalogs modulated adaptive immunity against  
393 SARS-CoV-2 in our experiments. While immunomodulation of adaptive immunity by rapalogs  
394 may provide benefit for patients already suffering from COVID-19, pre-existing rapalog use may  
395 enhance susceptibility by counteracting cell-intrinsic immunity.

396 The injection dose of rapamycin or ridaforolimus (3 mg/kg) that we administered once to  
397 hamsters or daily to mice, when adjusted for body surface area and an average human weight of  
398 60 kg [57], equates to approximately 15 mg per human. This figure is similar to those  
399 administered to humans in clinical settings, such as the use of rapamycin for the treatment of  
400 glioblastoma (up to 10 mg daily for multiple days), the use of temsirolimus for the treatment of  
401 renal cell carcinoma (25 mg once weekly), or the use of everolimus for the treatment of tuberous  
402 sclerosis (TS), a genetic disorder resulting in hyperactivation of mTOR (10 mg daily,  
403 continuously) [23, 58-60]. Interestingly, a case report detailed the deaths of two TS patients (a  
404 father and daughter) who, despite discontinuing everolimus upon detection of SARS-CoV-2  
405 infection, died from severe COVID-19 in late 2020 [60]. Our findings detailing the suppression  
406 of cell-intrinsic immunity by rapalogs raise the possibility that their use may predispose  
407 individuals to SARS-CoV-2 infection and severe forms of COVID-19. More generally, they  
408 provide new insight into how rapamycin and rapalogs may elicit unintended  
409 immunocompromised states and increase human susceptibility to multiple virus infections.

410 By leveraging the differential functional properties of rapalogs, we reveal how the  
411 mTOR-TFEB-lysosome axis impacts intrinsic resistance to SARS-CoV-2 infection. Specifically,  
412 rapamycin and select rapalogs (everolimus and temsirolimus) promote infection at the stage of  
413 cell entry, and this is functionally linked to nuclear accumulation of TFEB and the lysosomal  
414 degradation of IFITM proteins by endolysosomal microautophagy (**Figure 9**). While mTOR

415 phosphorylates TFEB at S211 to promote the sequestration of TFEB in the cytoplasm, the  
416 phosphatase calcineurin dephosphorylates TFEB at this position to promote nuclear translocation  
417 [61]. Therefore, the extent to which different rapalogs promote nuclear TFEB accumulation may  
418 be a consequence of differential mTOR inhibition and/or differential calcineurin activation.  
419 Calcineurin is activated by calcium release through the lysosomal calcium channel TRPML1  
420 (also known as mucolipin-1) [61], and interestingly, it was shown that rapamycin and  
421 temsirolimus, but not ridaforolimus, promote calcium release by TRPML1 [53]. Therefore, it is  
422 worth examining whether TRPML1 or related lysosomal calcium channels are required for the  
423 effects of rapalogs on virus infection. Overall, our findings reveal a previously unrecognized  
424 mechanism by which TFEB promotes virus infections—inhibition of cell-intrinsic defenses  
425 restricting virus entry. We show that nuclear TFEB induces the degradation of IFITM proteins,  
426 but it may also trigger the loss or relocalization of other antiviral factors that remain to be  
427 uncovered. Furthermore, TFEB-mediated induction of dependency factors, such as cathepsin L,  
428 is likely to partially contribute to the overall impact of rapalogs on SARS-CoV-2 infection.  
429 Overall, this work identifies TFEB as a therapeutic target, and inhibitors that limit levels of  
430 nuclear TFEB could be mobilized for broad-spectrum antiviral activity.

431 We previously demonstrated that treatment of cells with micromolar quantities of  
432 rapamycin induced the lysosomal degradation of IFITM2/3 via a pathway that is independent of  
433 macroautophagy yet dependent upon endosomal complexes required for transport (ESCRT)-  
434 mediated sorting of IFITM2/3 into intraluminal vesicles of late endosomes/MVB [37]. This  
435 MVB-mediated degradation pathway is also referred to as microautophagy, which occurs  
436 directly on endosomal or lysosomal membranes and involves membrane invagination [62]. In  
437 both yeast and mammalian cells, microautophagy is characterized by ESCRT-dependent sorting  
438 of endolysosomal membrane proteins into intraluminal vesicles followed by their degradation by  
439 lysosomal hydrolases [63]. While microautophagy selectively targets ubiquitinated  
440 endolysosomal membrane proteins, cytosolic proteins can also be non-selectively internalized  
441 into intraluminal vesicles and degraded [64, 65]. Interestingly, microautophagy is known to be  
442 regulated by mTOR [66, 67], and mTOR inhibition triggers a ubiquitin- and ESCRT-dependent  
443 turnover of vacuolar (lysosomal) membrane proteins in yeast [68, 69]. Overall, our findings  
444 suggest that select rapalogs induce a rapid, TFEB-dependent, endolysosomal membrane  
445 remodeling program known as microautophagy, and IFITM proteins are among the client  
446 proteins subjected to this pathway. The full cast of cellular factors that orchestrate this selective  
447 degradation program in mammalian cells and the other client proteins subjected to it will need to  
448 be worked out. Interestingly, the E3 ubiquitin ligase NEDD4 was previously shown to  
449 ubiquitinate IFITM2 and IFITM3 and to induce their lysosomal degradation in mammalian cells  
450 [70, 71], while Rsp5, the yeast ortholog of NEDD4, was shown to ubiquitinate vacuolar proteins  
451 turned over by microautophagy in yeast [72]. Therefore, rapamycin and select rapalogs may  
452 upregulate NEDD4 function, resulting in selective degradation of a subset of the cellular  
453 proteome that includes IFITM proteins. Indeed, NEDD4 and the related NEDD4L are among the  
454 known target genes regulated by TFEB [73].

455 The relationship between IFITM proteins and human coronaviruses is complex. It was  
456 previously shown that IFITM3 facilitates replication of the seasonal coronavirus hCoV-OC43  
457 [74], while we and others recently showed that SARS-CoV-1 and SARS-CoV-2 infection is  
458 inhibited by ectopic and endogenous IFITM1, IFITM2, and IFITM3 from mice and humans [75-  
459 79]. Intriguingly, mutants of human IFITM3 that lack the capacity to internalize into endosomes  
460 lost antiviral activity and promoted SARS-CoV-2 and MERS-CoV infection, revealing that

461 IFITM3 can either inhibit or enhance infection depending on its subcellular localization [75, 80].  
462 Furthermore, one study reported that endogenous human IFITM proteins promoted infection by  
463 SARS-CoV-2 in certain human tissues [48]. Overall, the net effect of human IFITM proteins on  
464 SARS-CoV-2 infection *in vivo* remains unclear. However, the impact of rapamycin in our  
465 experimental SARS-CoV-2 infections of hamsters and mice suggests that rapamycin-mediated  
466 loss of IFITM proteins favors virus infection and viral disease, consistent with IFITM proteins  
467 performing antiviral roles against SARS-CoV-2 in those species. Accordingly, it was recently  
468 demonstrated that mouse IFITM3 protects mice from viral pathogenesis following MA SARS-  
469 CoV-2 infection [81].

470 Other lines of evidence support an antiviral role for IFITM proteins during SARS-CoV-2  
471 infection in humans. While SARS-CoV-2 infection has been shown to cause deficiencies in  
472 interferon synthesis and interferon response pathways, administration of type I interferon *in vivo*  
473 promotes SARS-CoV-2 clearance in hamsters and humans [82]. Notably, IFITM3 is among the  
474 most highly induced genes in primary human lung epithelial cells exposed to SARS-CoV-2 [83,  
475 84], and humans experiencing mild or moderate COVID-19 showed elevated induction of  
476 antiviral genes, including *IFITM1* and *IFITM3*, in airway epithelium compared to individuals  
477 suffering from more severe COVID-19 [85]. Single nucleotide polymorphisms in human *IFITM3*  
478 known as ns12252 and rs34481144, which lead to IFITM3 loss-of-function, have been associated  
479 with severe outcomes following Influenza A virus infection as well as severe COVID-19 [86,  
480 87]. These data suggest that cell-intrinsic immunity in airways plays a role in restricting virus  
481 spread and constraining systemic pathology during infection. Therefore, downmodulation of  
482 IFITM proteins by select rapalogs may contribute to the immunocompromised state that these  
483 drugs are well known to elicit in humans. This possibility warrants the close examination of  
484 different rapalog regimens on respiratory virus acquisition and disease in humans.

485

## 486 **Materials and Methods**

487

### 488 **Cell lines, cell culture, inhibitors, and cytokines**

489

490 HEK293T (CRL-3216) and Calu-3 (HTB-55) cells were obtained from ATCC. HeLa-ACE2,  
491 HeLa-DPP4, and A549-ACE2 cell lines were produced by transducing cells with lentivirus  
492 packaging pWPI encoding ACE2 or DPP4 and selecting with blasticidin. HeLa IFITM1/2/3  
493 Knockout (C5-9) cells were purchased from ATCC (CRL-3452). HeLa *TFEB* KO cells were  
494 kindly provided by Ramnik J. Xavier (Broad Institute) and were described in [88]. Primary  
495 human small airway (lung) epithelial cells (HSAEC) were purchased from ATCC (PCS-301-  
496 010). The partially immortalized nasal epithelial cell line (UNCNN2TS) was kindly provided by  
497 Scott H. Randell (University of North Carolina School of Medicine). Vero E6 cells (NR-53726)  
498 were obtained from BEI Resources. Vero-TMPRSS2 cells were a kind gift from Shan-Lu Liu  
499 (The Ohio State University). All cells were cultured at 37°C with 5% CO<sub>2</sub> in Dulbecco's  
500 Modified Eagle Medium (DMEM) supplemented with 10% fetal bovine serum (HyClone,  
501 Cytiva), except for UNCNN2TS, which were cultured in EpiX Medium (Propagenix), and  
502 HSAEC, which were cultured with airway epithelial cell basal medium (ATCC, PCS-300-030)  
503 and the bronchial epithelial cell growth kit (ATCC, PCS-300-040). Rapamycin (553211) was  
504 obtained from Sigma. Everolimus (S1120), temsirolimus (S1044), ridaforolimus (S5003),  
505 tacrolimus (S5003), and SAR405 (S7682) were obtained from Selleckchem. U18666A (U3633)

506 and Bafilomycin A1 (SML1661) were obtained from Sigma. Type-I interferon (human  
507 recombinant interferon-beta<sub>ser17</sub>, NR-3085) was obtained from BEI Resources.

508

### 509 **Plasmids and RNA interference**

510

511 pcDNA3.1 encoding human ACE2 was kindly provided by Thomas Gallagher (Loyola  
512 University). pcDNA3.1 encoding CoV-1 Spike or CoV-2 Spike tagged with a C9 epitope on the  
513 C-terminus, or MERS Spike, was kindly provided by Thomas Gallagher (Loyola University).  
514 pcDNA3.1 encoding CoV-1 Spike or CoV-2 Spike tagged with a FLAG epitope on the C-  
515 terminus was obtained from Michael Letko and Vincent Munster (NIAID). pMD2.G encoding  
516 VSV-G (12259) was obtained from Addgene (a generous gift from Didier Trono). pWPI was  
517 obtained from Addgene (12254) and human ACE2 or human TMPRSS2 was introduced by  
518 Gateway cloning (Gateway LR Clonase II Enzyme mix (11791020)) as per manufacturer's  
519 instructions. pPolII encoding hemagglutinin (HA) or neuraminidase (NA) from Influenza  
520 A/Turkey/1/2005 (H5N1) were kindly provided by Richard Yi Tsun Kao (The University of  
521 Hong Kong). pCMV encoding HIV-1 Vpr fused to beta lactamase (pCMV4-BlaM-Vpr) was  
522 obtained from Addgene (21950). A plasmid encoding replication-incompetent HIV-1 lacking *env*  
523 and *vpr* and encoding luciferase (pNL4-3LucR-E-) was kindly provided by Vineet KewalRamani  
524 (National Cancer Institute). A plasmid encoding replication-incompetent HIV-1 lacking *env*  
525 (pNL4-3E-) was kindly provided by Olivier Schwartz (Institut Pasteur). pEGFP-N1-TFEB  
526 (38119) and pEGF-N1-Δ30TFEB (44445) were obtained from Addgene (a generous gift of  
527 Shawn M. Ferguson). pEGFP-2xFYVE (140047) was obtained from Addgene (a gift from  
528 Harald Stenmark). Silencer Select siRNA targeting IFITM3 (s195035) and a non-targeting  
529 control (No. 1) was obtained from Ambion. Cells were transfected with 20 nM siRNA using  
530 Opti-MEM (Gibco) and Lipofectamine RNAiMAX (Thermo Fisher).

531

### 532 **Virus and pseudovirus infections**

533

534 SARS-CoV-2 isolate USA-WA1/2020 (MN985325.1) was provided by the Centers for Disease  
535 Control or by BEI Resources (NR-52281). Virus propagation was performed in Vero E6 cells.  
536 Mouse-adapted (MA) SARS-CoV-2 variant MA10 (in the USA-WA1/2020 backbone) [89] was  
537 obtained from BEI Resources (NR-55329). Virus propagation was performed in Vero E6 cells  
538 and subsequently in Vero-TMPRSS2 cells. Virus was sequenced to ensure lack of tissue culture  
539 adaptations, including furin cleavage site mutations. Virus titers were calculated by plaque assay  
540 performed in Vero E6 cells as follows: serial 10-fold dilutions were added to Vero E6  
541 monolayers in 48-well plates for 1 hour at 37°C. Cells were overlaid with 1.5% carboxymethyl  
542 cellulose (Sigma) in modified Eagle's medium containing 3% fetal bovine serum (Gibco), 1 mM  
543 L-glutamine, 50 units per mL penicillin and 50 µg per mL streptomycin. Three days post-  
544 infection, cells were fixed in 10% formalin and stained with crystal violet to visualize and count  
545 plaques as previously described [90]. Titers were calculated as plaque forming units per mL and  
546 normalized as described in the figure captions. HIV-based pseudovirus was produced by  
547 transfecting HEK293T cells with 12 µg of pNL4-3LucR-E- and 4 µg of plasmid encoding viral  
548 glycoproteins (pcDNA3.1 Spike (CoV-1, CoV-2, or MERS), pMD2.G-VSV-G, or 2 µg of  
549 pPolII-HA and 2 µg of pPolII-NA) using TransIT-293 (Mirus). Virus supernatant was  
550 harvested 72 hours post-transfection and filtered through 0.22 µm filters. Pseudovirus titers were  
551 determined by p24 ELISA (XpressBio) and 100 ng p24 equivalent was added to target cells and

552 incubated for 72 hours prior to lysis with Passive Lysis Buffer (Promega). Luciferase activity  
553 was measured using the Luciferase Assay System (Promega). VSV-based pseudovirus was  
554 produced as previously described [91]. In brief, HEK293T cells were transfected with 2 µg  
555 pcDNA3.1 CoV-2 Spike using Lipofectamine2000 (Thermo Fisher). At 24 hours post-  
556 transfection, culture medium was removed from cells and 2 mL of VSV-luc/GFP + VSV-G (seed  
557 particles) was added. At 48 hours post-infection, virus supernatants were collected, clarified by  
558 centrifugation at 500xG for 5 mins, and stored. 50 µL of virus supernatants were added to target  
559 cells for a period of 24 hours prior to fixation with 4% paraformaldehyde (for measurements of  
560 GFP+ cells with flow cytometry). For infections with replication-competent SARS-CoV-2,  
561 rapamycin, everolimus, temsirolimus, or ridaforolimus (20 µM) were used to pretreat cells for 4  
562 hours and then drugs were washed away prior to addition of virus at a multiplicity of infection  
563 (MOI) of 0.1. DMSO (Sigma) was used as a vehicle control. At one hour post-virus addition,  
564 cells were washed once with 1X PBS and overlaid with complete medium. Supernatants were  
565 harvested 24 hours later, and titers were determined on plaque assays performed in Vero E6  
566 cells. For single-round infections using HIV- or VSV-based pseudovirus, rapamycin, everolimus,  
567 temsirolimus, ridaforolimus, or tacrolimus (20 µM) were used to pretreat cells for 4 hours and  
568 were maintained for the duration of infection and until harvest of cells for luciferase assay or  
569 flow cytometry. DMSO (Sigma) was used as a vehicle control.

570

#### 571 **FRET-based virus entry assay**

572

573 HIV-based pseudovirus incorporating BlaM-Vpr and CoV-2 Spike was produced by transfecting  
574 HEK293T cells with pNL4-3E- (15 µg), pCMV4-BlaM-Vpr (5 µg), and pcDNA3.1 CoV-2 Spike  
575 (5 µg) using the calcium phosphate technique. Briefly, six million 293T cells were seeded in a  
576 T75 flask. Plasmid DNA was mixed with sterile H<sub>2</sub>O, CaCl<sub>2</sub>, and Tris-EDTA (TE) buffer, and  
577 the totality was combined with Hepes-buffered saline (HBS). The transfection volume was added  
578 dropwise, and cells were incubated at 37°C for 48 h. Supernatants were recovered and clarified  
579 by centrifugation, passed through a 0.45 µm filter, and stored. Titers were measured using an  
580 HIV-1 p24 ELISA kit (XpressBio). 50 ng p25 equivalent of virus was added to HeLa-ACE2 cells  
581 for 2 hours. Cells were washed and labeled with the CCF2-AM β-lactamase Loading Kit  
582 (Invitrogen) for 2 hours and analyzed for CCF2 cleavage by flow cytometry as described [92].  
583 Rapamycin, everolimus, temsirolimus, or ridaforolimus (20 µM) were used to pretreat cells for 4  
584 hours prior to virus addition and were maintained for the duration of infection. DMSO (Sigma)  
585 was used as a vehicle control.

586

#### 587 **Western blot, antibodies, and flow cytometry**

588 Whole cell lysis was performed with RIPA buffer (Thermo Fisher) supplemented with Halt  
589 Protease Inhibitor EDTA-free (Thermo Fisher). Lysates were clarified by centrifugation and  
590 supernatants were collected and stored. Protein concentration was determined with the Protein  
591 Assay Kit II (Bio-Rad), and 10-15 µg of protein was loaded into 12% acrylamide Criterion XT  
592 Bis-Tris Precast Gels (Bio-Rad). Electrophoresis was performed with NuPage MES SDS  
593 Running Buffer (Invitrogen) and proteins were transferred to Amersham Protran Premium  
594 Nitrocellulose Membrane, pore size 0.20 µm (GE Healthcare). Membranes were blocked with  
595 Odyssey Blocking Buffer (Li-COR) and incubated with the following primary antibodies diluted  
596 in Odyssey Antibody Diluent (Li-COR): anti-IFITM1 (60074-1-Ig; Proteintech), anti-IFITM2

597 (66137-1-Ig; Proteintech), anti-IFITM3 (EPR5242, ab109429; Abcam), anti-Fragilis (ab15592;  
598 Abcam (detects murine IFITM3)), anti-IFITM2/3 (66081-1-Ig; Proteintech), anti-actin (C4, sc-  
599 47778; Santa Cruz Biotechnology), anti-hACE2 (ab15348; Abcam), anti-TFEB (4240S; Cell  
600 Signaling Technology), and anti-pTFEB (Ser211) (37681S; Cell Signaling Technology).  
601 Secondary antibodies conjugated to DyLight 800 or 680 (Li-Cor) and the Li-Cor Odyssey CLx  
602 imaging system were used to reveal specific protein detection. Images were analyzed (including  
603 signal quantification) and assembled using ImageStudioLite (Li-Cor). Cell viability was  
604 measured using LIVE/DEAD Red Dead Cell Stain Kit (Thermo Fisher). Cells were fixed and  
605 permeabilized with Cytofix/Cytoperm reagent (BD) for 20 minutes and washed in Perm/Wash  
606 buffer (BD). Flow cytometry was performed on an LSRFortessa (BD).

## 607 **Confocal fluorescence and immunofluorescence microscopy**

608  
609 HeLa-ACE2 cells were fixed with 4% paraformaldehyde, stained with anti-IFITM2/3 (66081-1-  
610 Ig; Proteintech), goat anti-mouse IgG Alexa Fluor 647 (A21235; Thermo Fisher) and DAPI  
611 (62248; Thermo Fisher), and imaged in a glass-bottom tissue culture plate with an Operetta CLS  
612 High-Content Analysis System (Perkin Elmer). For measurement of TFEB-GFP  
613 nuclear/cytoplasmic distribution, HeLa-ACE2 cells were transfected with pEGFP-N1-TFEB for  
614 24 hours, fixed with 4% paraformaldehyde, stained with HCS CellMask Red Stain (H32712;  
615 Thermo Fisher) and DAPI, and imaged with an Operetta CLS. Using Harmony software (Perkin  
616 Elmer), nuclear/cytoplasmic ratios of TFEB-GFP were calculated in single cells as follows: cells  
617 were delineated by CellMask Red Stain, nuclei were delineated by DAPI, nuclear TFEB-GFP  
618 was designated as GFP overlapping with DAPI, and cytoplasmic TFEB-GFP was designated as  
619 total GFP signal minus nuclear TFEB-GFP. Average ratios were calculated from 20-30 cells per  
620 field, and the mean of averages from 10 fields was obtained (total of approximately 250 cells per  
621 condition). For measurement of IFITM2/3 levels in cells transfected with TFEB $\Delta$ 30-GFP, HeLa-  
622 ACE2 cells were transfected with pEGF-N1- $\Delta$ 30TFEB for 24 hours, fixed and permeabilized  
623 with BD Cytofix/Cytoperm (Fisher Scientific), stained with anti-IFITM2/3 and goat anti-mouse  
624 IgG Alexa Fluor 647, and imaged with an Operetta CLS. The IFITM2/3 fluorescence intensity  
625 within a single, medial Z section was measured in approximately 150 GFP-negative cells and  
626 150 GFP-positive cells using the freehand selections tool in ImageJ.

627

## 628 **In vivo infections of hamsters and mice with SARS-CoV-2**

629

630 Male Golden Syrian hamsters between the ages of 6-8 weeks were acclimated for 11 days  
631 following receipt. Hamsters received an intraperitoneal injection (500  $\mu$ L) of rapamycin (HY-  
632 10219; MedChemExpress) or ridaforolimus (HY-50908; MedChemExpress) at 3 mg/kg or an  
633 equivalent amount of DMSO (8 hamsters per group). Four hours later, hamsters were challenged  
634 with  $6 \times 10^3$  plaque forming units of SARS-CoV-2 isolate USA-WA1/2020 (amplified on Calu-3  
635 cells) through intranasal inoculation (50  $\mu$ L in each nare). Half of the hamsters in each group  
636 received a second injection at day 2 post-infection. Clinical observations and weights were  
637 recorded daily up until day 10 post-infection. According to Institutional Animal Care and Use  
638 Committee human euthanasia criteria, hamsters were euthanized immediately if weight loss  
639 exceeded 20%. Otherwise, hamsters were euthanized on day 10 post-infection. Oral swabs were  
640 collected on day 2 post-infection for measurement of viral RNA by quantitative PCR of the viral  
641 N (nucleocapsid) gene. Lungs were harvested following euthanasia (day 10 or earlier) and

642 infectious viral load was determined by TCID<sub>50</sub> assay in Vero-TMPRSS2 cells. C57BL/6 mice  
643 received an intraperitoneal injection of 3 mg/kg rapamycin (NC9362949; LC-Laboratories) or an  
644 equivalent amount of DMSO (7 and 6 mice per group, respectively). The following day, mice  
645 were challenged intranasally with 6 x 10<sup>4</sup> TCID<sub>50</sub> equivalent of MA10 SARS-CoV-2 (USA-  
646 WA1/2020 backbone). Mice received a second injection of rapamycin or DMSO on the day of  
647 infection and a third on day one post-infection. Mice were euthanized for lung harvest on day  
648 two post-infection. Infectious viral load was determined by TCID<sub>50</sub> assay in Vero-TMPRSS2  
649 cells. Animal studies were conducted in compliance with all relevant local, state, and federal  
650 regulations and were approved by the Institutional Animal Care and Use Committee of Bioqual  
651 and of the Ohio State University.

652

## 653 **Figure Legends**

654

655 **Figure 1: Rapamycin and its analogs share a macrolide structure but differ by the**  
656 **functional group present at carbon-40.** Violet and green bubbles indicate the FKBP- and  
657 mTOR-binding sites, respectively.

658 **Figure 2: Rapalogs promote SARS-CoV-2 infection in lung epithelial cells to different**  
659 **extents by counteracting the intrinsic antiviral state** (A) A549-ACE2 were treated with or  
660 without type I interferon (250 U/mL) for 18 hours and then treated with 20 μM rapamycin (Rap),  
661 everolimus (Eve), temsirolimus (Tem), ridaforolimus (Rid), or an equivalent volume of DMSO  
662 (D) for 4 hours. HIV-CoV-2 (100 ng p24 equivalent) was added to cells and infection was  
663 measured by luciferase activity at 48 hours post-infection. Luciferase units were normalized to  
664 100 in the DMSO condition in the absence of interferon. (B) A549-ACE2 cells from (A) were  
665 subjected to SDS-PAGE and Western blot analysis. Immunoblotting was performed with anti-  
666 IFITM2/3, anti-ACE2, and anti-actin (in that order) on the same nitrocellulose membrane.  
667 Numbers and tick marks indicate size (kilodaltons) and position of protein standards in ladder.  
668 (C) Primary HSAEC were treated with 20 μM Rap, Eve, Tem, Rid, or an equivalent volume of  
669 DMSO for 4 hours. VSV-CoV-2 (50 μL) was added to cells and infection was measured by GFP  
670 expression at 24 hours post-infection using flow cytometry. (D) A549-ACE2 were treated with  
671 varying concentrations of Eve or DMSO (equivalent to 30 μM of Eve) for 4 hours. SARS-CoV-2  
672 (nCoV-WA1-2020; MN985325.1) was added to cells at an MOI of 0.1 and infectious titers were  
673 measured in VeroE6 cells by calculating the TCID<sub>50</sub> per mL of supernatants recovered at 24  
674 hours post-infection. TCID<sub>50</sub> per mL values were normalized to 100 in the DMSO condition.  
675 Means and standard error were calculated from 3-5 experiments. Statistical analysis was  
676 performed with one-way ANOVA and asterisks indicate significant difference from DMSO. \*, p  
677 < 0.05; \*\*, p < 0.01. Rel.; relative.

678 **Figure 3: Rapalogs promote SARS-CoV-2 infection in HeLa-ACE2 cells.** (A) HeLa-ACE2  
679 were treated with varying concentrations of Eve or DMSO for 4 hours. SARS-CoV-2 (nCoV-  
680 WA1-2020; MN985325.1) was added to cells at an MOI of 0.1 and infectious titers were  
681 measured in VeroE6 cells by calculating the TCID<sub>50</sub> of supernatants recovered at 24 hours post-  
682 infection. TCID<sub>50</sub> per mL values were normalized to 100 in the DMSO condition. (B) HeLa-  
683 ACE2 were treated with 20 μM Rap, Eve, Tem, Rid, or an equivalent volume of DMSO for 4  
684 hours. SARS-CoV-2 (nCoV-WA1-2020; MN985325.1) was added to cells at an MOI of 0.1 and  
685 infectious titers were measured in VeroE6 cells by calculating the TCID<sub>50</sub> per mL of

686 supernatants recovered at 24 hours post-infection. TCID<sub>50</sub> per mL values were normalized to 100  
687 in the DMSO condition. (C) HeLa-ACE2 were treated with 20 μM Rap, Eve, Tem, Rid, or an  
688 equivalent volume of DMSO for 4 hours. HIV-CoV-2 (100 ng p24 equivalent) was added to cells  
689 and infection was measured by luciferase activity at 48 hours post-infection. Luciferase units  
690 were normalized to 100 in the DMSO condition. (D) HeLa-ACE2 cells from (C) were subjected  
691 to SDS-PAGE and Western blot analysis. Immunoblotting was performed with anti-IFITM2,  
692 anti-IFITM1, anti-IFITM3, anti-ACE2, and anti-actin (in that order) on the same nitrocellulose  
693 membrane. (E) IFITM3 levels from (D) were normalized to actin levels and summarized from 5  
694 independent experiments. (F) HeLa-ACE2 were treated with 20 μM Rap, Eve, Tem, Rid, or an  
695 equivalent volume of DMSO for 4 hours and cells were fixed, stained with DAPI and anti-  
696 IFITM2/3, and imaged by confocal immunofluorescence microscopy. Images represent stacks of  
697 5 Z-slices and one representative image is shown per condition. Means and standard error were  
698 calculated from 3-5 experiments. Statistical analysis was performed with one-way ANOVA and  
699 asterisks indicate significant difference from DMSO. \*, p < 0.05; \*\*, p < 0.01. Rel.; relative.

700  
701 **Figure 4: Rapalogs promote cell entry mediated by diverse viral fusion proteins.** (A) HeLa-  
702 ACE2 were treated with 20 μM Rap, Eve, Tem, Rid, or an equivalent volume of DMSO for 4  
703 hours. HIV-CoV-2 S pseudovirus incorporating BlaM-Vpr (HIV-BlaM-CoV-2) was added to  
704 cells for 2 hours and washed. Cells were incubated with CCF2-AM for an additional 2 hours and  
705 fixed. Cleaved CCF2 was measured by flow cytometry. Dot plots visualized as density plots  
706 from one representative experiment are shown on the left and the percentage of CCF2+ cells  
707 which exhibit CCF2 cleavage is indicated. Summary data representing the average of four  
708 experiments is shown on the right. (B) HIV-CoV-1, (C) HIV-MERS-CoV, (D) HIV-IAV HA, or  
709 (E) HIV-VSV G were added to HeLa-ACE2 or HeLa-DPP4 cells as in (A) and infection was  
710 measured by luciferase activity at 48 hours post-infection. Luciferase units were normalized to  
711 100 in the DMSO condition. Means and standard error were calculated from 3-4 experiments.  
712 Statistical analysis was performed with one-way ANOVA and asterisks indicate significant  
713 difference from DMSO. \*, p < 0.05; \*\*, p < 0.01. Rel.; relative.

714  
715 **Figure 5: Select rapalogs enhance Spike-mediated infection in HeLa-ACE2 by inhibiting**  
716 **IFITM2 and IFITM3.** (A) HeLa WT and HeLa *IFITM1-3* KO cells were transiently transfected  
717 with 0.150 μg pcDNA3.1-hACE2 for 24 hours. Whole cell lysates were subjected to SDS-PAGE  
718 and Western blot analysis. Immunoblotting was performed with anti-IFITM2, anti-IFITM3, anti-  
719 IFITM1, anti-ACE2, and anti-actin (in that order) on the same nitrocellulose membrane. (B)  
720 HeLa *IFITM1-3* KO were transfected with IFITM2 or IFITM2 and IFITM3 and SDS-PAGE and  
721 Western blot analysis was performed. (C) HIV-CoV-2 was added to transfected cells from (B)  
722 and infection was measured by luciferase activity at 48 hours post-infection. Luciferase units  
723 were normalized to 100 in HeLa WT cells treated with DMSO. Means and standard error were  
724 calculated from 5 experiments. Statistical analysis was performed with one-way ANOVA and  
725 asterisks indicate significant difference from nearest DMSO condition. \*, p < 0.05; \*\*, p < 0.01.  
726 Rel.; relative.

727  
728 **Figure 6: Nuclear TFEB triggers IFITM2/3 turnover, promotes Spike-mediated infection,**  
729 **and is required for enhancement of infection by rapalogs.** (A) A549-ACE2 were treated with  
730 20 μM Rap, Eve, Tem, Rid, or tacrolimus (Tac) for 4 hours and whole cell lysates were  
731 subjected to SDS-PAGE and Western blot analysis. Immunoblotting was performed with anti-



732 TFEB and anti-pTFEB (S211). (B) pTFEB (S211) levels were divided by total TFEB levels and  
733 summarized as an average of 3 experiments. (C) HeLa-ACE2 were transfected with TFEB-GFP  
734 for 24 hours, treated with Rap, Eve, Tem, Rid or Tac for 4 hours, stained with DAPI and  
735 CellMask, and imaged by high-content confocal fluorescence microscopy. Representative  
736 images from each condition are shown (DAPI and CellMask channels are not shown). (D) The  
737 ratio of nuclear to cytoplasmic TFEB-GFP was calculated in individual cells and the average  
738 ratio derived from 50-100 cells per condition is shown. (E) HeLa-ACE2 were transfected with  
739 0.5  $\mu$ g TFEB $\Delta$ 30-GFP for 24 hours, fixed, stained with anti-IFITM2/3, and imaged by confocal  
740 immunofluorescence microscopy. A representative field is shown on the left. The average  
741 intensity of IFITM2/3 levels in approximately 150 GFP-negative and 150 GFP-positive cells  
742 were grouped and summarized from two independent transfections on the right. (F) HeLa-ACE2  
743 were transfected with 0.5  $\mu$ g TFEB $\Delta$ 30-GFP, or not transfected, for 24 hours and HIV-CoV-2  
744 (100 ng p24 equivalent) was added to cells. Infection was measured by luciferase activity at 48  
745 hours post-infection. Luciferase units were normalized to 100 in the non-transfected condition.  
746 (G) HeLa WT or HeLa *TFEB* KO were transfected with 0.3  $\mu$ g pcDNA3.1-hACE2 for 24 hours  
747 and treated with 20  $\mu$ M Rap, Eve, Tem, Rid, or a corresponding volume of DMSO for 4 hours.  
748 HIV-CoV-2 (100 ng p24 equivalent) was added to cells and infection was measured by luciferase  
749 activity at 48 hours post-infection. Luciferase units were normalized to 100 in the non-  
750 transfected condition. Means and standard error were calculated from 3 experiments, except for  
751 TFEB-GFP imaging experiments, for which 2 experiments (transfections) were performed.  
752 Statistical analysis was performed with one-way ANOVA and asterisks indicate significant  
753 difference from DMSO. \*,  $p < 0.05$ ; \*\*,  $p < 0.01$ . Rel.; relative. A.u.; arbitrary units.  
754

755 **Figure 7: Rapamycin injection into hamsters intensifies viral disease during SARS-CoV-2**  
756 **infection.** (A) Schematic of intraperitoneal injections and intranasal SARS-CoV-2 challenge in  
757 hamsters. Golden Syrian hamsters were injected with 3 mg/kg Rap, Rid, or equivalent amounts  
758 of DMSO (4 animals per group). Four hours later, hamsters were infected intranasally with  $6 \times$   
759  $10^3$  plaque forming units of SARS-CoV-2. At 2 days post-infection, half of the animals received  
760 a second injection of Rap, Rid, or DMSO. Oral swabs were taken and used for measurement of  
761 oral viral RNA load by qPCR. At 10 days post-infection (or earlier, if more than 20% of weight  
762 loss occurred), hamsters were euthanized, and lungs were harvested for determination of  
763 infectious virus titer by TCID<sub>50</sub> assay in Vero-TMPRSS2 cells (B) Mean body weight and  
764 standard error for each treatment group is plotted by day post-infection. (C) Kaplan-Meier  
765 survival curves were generated according to the dates of euthanasia (or in one case, when an  
766 animal was found dead). (D) Viral RNA copy number was determined by qPCR from oral swab  
767 at 2 days post-infection. Data is depicted as box and whiskers plots. (E) Infectious virus titers in  
768 lungs were determined by TCID<sub>50</sub> in Vero-TMPRSS2 cells. Data is depicted as floating bars and  
769 is grouped by brackets according to hamsters that survived until 10 days post-infection and those  
770 that were euthanized at 7 days post-infection. Statistical analysis in (B) was performed by  
771 student's T test and asterisks indicate significant difference from DMSO (gray asterisks for Rap  
772 and black asterisks for Rid). Statistical analysis in (C) was performed by comparing survival  
773 curves between Rap and DMSO or Rid and DMSO using the Log-rank (Mantel-Cox) test.  
774 Illustration created with BioRender.com.  
775

776 **Figure 8: Rapamycin injection into mice downmodulates IFITM3 in lungs and boosts MA**  
777 **SARS-CoV-2 titers in lungs.** (A) Schematic of intraperitoneal injections and intranasal mouse-

778 adapted (MA) SARS-CoV-2 challenge in mice. C57BL/6 mice were injected with 3 mg/kg of  
779 Rap or an equivalent amount of DMSO (6 or 7 mice per group, respectively). The following day,  
780 mice were infected intranasally with  $6 \times 10^4$  TCID<sub>50</sub> MA SARS-CoV-2. Mice received second  
781 and third injections of Rap or DMSO on the day of infection and on day 1 post-infection,  
782 respectively. (B) Lungs were harvested from infected mice upon euthanasia at day 2 post-  
783 infection and infectious viral loads were determined by TCID<sub>50</sub> in Vero-TMPRSS2 cells.  
784 Geometric mean TCID<sub>50</sub> per gram was calculated per treatment group and data is depicted as box  
785 and whiskers plots. Statistical analysis was performed with Mann-Whitney test and asterisks  
786 indicate significant difference from DMSO. \*,  $p < 0.05$ ; \*\*,  $p < 0.01$ . (C) Lung homogenates (3  
787  $\mu$ g) from mice injected with Rap or DMSO were subjected to SDS-PAGE and Western blot  
788 analysis. Immunoblotting was performed with anti-Fragilis/IFITM3 (ab15592) and anti-actin.  
789 Illustration created with BioRender.com.

790

791 **Figure 9:** Model for rapalog-mediated enhancement of SARS-CoV-2 infection. Rapamycin and  
792 rapalogs everolimus and temsirolimus potently inhibit the phosphorylation of TFEB by mTOR,  
793 while ridaforolimus does not. As a result, TFEB translocates into the nucleus and induces genes  
794 functioning in lysosomal activities, including autophagy-related pathways. Nuclear TFEB  
795 triggers a microautophagy pathway that results in accelerated degradation of membrane proteins  
796 IFITM2 and IFITM3. Loss of IFITM2/3 promotes SARS-CoV-2 entry into cells by facilitating  
797 fusion between viral membranes and cellular membranes. Illustration created with  
798 BioRender.com.

799 **Supplemental Figure 1:** (A) A549-ACE2 cells were treated with 20  $\mu$ M Rap, Eve, Rid, Tem, or  
800 an equivalent volume of DMSO (in the absence of type-I interferon) for 4 hours and whole cell  
801 lysates were subjected to SDS-PAGE and Western blot analysis. Immunoblotting was performed  
802 with anti-IFITM2/3 and anti-actin. (B) Primary HSAEC were treated with 20  $\mu$ M Rap, Eve,  
803 Tem, Rid, or an equivalent volume of DMSO for 4 hours and whole cell lysates were subjected  
804 to SDS-PAGE and Western blot analysis. Immunoblotting was performed with anti-IFITM2 (not  
805 detected), anti-IFITM3, anti-IFITM1, and anti-actin. (C) Primary HSAEC were transfected with  
806 siRNA targeting IFITM3 or control siRNA for 48 hours. VSV-CoV-2 (50  $\mu$ L) was added to cells  
807 and infection was measured by GFP expression at 24 hours post-infection using flow cytometry.  
808 siRNA-transfected cells were subjected to SDS-PAGE and Western blot analysis.  
809 Immunoblotting was performed with anti-IFITM2 (not detected), anti-IFITM3, anti-IFITM1, and  
810 anti-actin. (D) Semi-transformed nasal epithelial cells (UNCNN2TS) were treated with 20  $\mu$ M  
811 Rap, Eve, Tem, Rid, or an equivalent volume of DMSO for 4 hours and whole cell lysates were  
812 subjected to SDS-PAGE and Western blot analysis. Immunoblotting was performed with anti-  
813 IFITM2 (not detected), anti-IFITM3, anti-IFITM1, and anti-actin. Immunoblots are  
814 representative of 3 independent experiments. Means and standard error were calculated from 3  
815 experiments. Statistical analysis was performed with student's T test and asterisks indicate  
816 significant difference from control siRNA. \*,  $p < 0.05$ ; \*\*,  $p < 0.01$ . Rel.; relative.

817 **Supplemental Figure 2:** (A) HeLa-ACE2 were treated with 20  $\mu$ M Rap, Eve, Tem, Rid, or an  
818 equivalent volume of DMSO for 24 hours and whole cell lysates were subjected to SDS-PAGE  
819 and Western blot analysis. Immunoblotting was performed with anti-IFITM2/3 and anti-actin.  
820 (B) HeLa-ACE2 were treated with 20  $\mu$ M Rap, Eve, Tem, Rid, or an equivalent volume of  
821 DMSO, in the presence or absence of 1  $\mu$ M Bafilomycin A1, for 4 hours and whole cell lysates

822 were subjected to SDS-PAGE and Western blot analysis. Immunoblotting was performed with  
823 anti-IFITM2, anti-IFITM1, anti-IFITM3, and anti-actin (in that order) on the same nitrocellulose  
824 membrane. (C) HeLa-ACE2 cells were transfected with FYVE-GFP for 24 hours followed by  
825 treatment with 100 nM SAR405 or an equivalent volume of ethanol (vehicle) for 3 hours. Cells  
826 were fixed and imaged by confocal immunofluorescence microscopy. For each condition, a Z-  
827 stack of 25 slices is shown as a maximum intensity projection. (D) HeLa-ACE2 were treated  
828 with 20  $\mu$ M Rap, Eve, Tem, Rid, or an equivalent volume of DMSO in the presence or absence  
829 of 100 nM SAR405 for 4 hours and whole cell lysates were subjected to SDS-PAGE and  
830 Western blot analysis. Immunoblotting was performed with anti-IFITM2/3 and anti-actin on the  
831 same nitrocellulose membrane. (E) HeLa-ACE2 were treated with 20  $\mu$ M Rap, Eve, Tem, Rid, or  
832 an equivalent volume of DMSO in the presence of 1  $\mu$ M Bafilomycin A1, 5  $\mu$ g/mL U18666A, or  
833 neither, for 4 hours. Cells were then fixed, permeabilized, and stained with anti-IFITM2/3.  
834 IFITM2/3 protein levels were measured using flow cytometry. Means and standard error were  
835 calculated from 3 experiments. Statistical analysis was performed with one-way ANOVA and  
836 asterisks indicate significant difference from DMSO. \*,  $p < 0.05$ ; \*\*,  $p < 0.01$ . Rel.; relative. All  
837 immunoblots are representative of three independent experiments.  
838

839 **Supplemental Figure 3:** (A) HeLa-ACE2 cells were transfected with 0.3  $\mu$ g pcDNA3.1-hACE2  
840 for 24 hours and treated with 20  $\mu$ M Rap, Eve, Tem, Rid, or the equivalent volume of DMSO for  
841 4 hours and whole cell lysates were subjected to SDS-PAGE and Western blot analysis. Cells  
842 were fixed, permeabilized, stained with anti-ACE2, and imaged by confocal  
843 immunofluorescence microscopy. Images represent a single, medial Z section. (B) HeLa-ACE2  
844 cells were treated with 20  $\mu$ M Rap, Eve, Tem, Rid, or the equivalent volume of DMSO for 4  
845 hours and subsequently fixed and stained with LIVE/DEAD Fixable Red Dead Cell Stain Kit for  
846 30 minutes according to manufacturer's instructions. Cells were analyzed by flow cytometry.  
847 Means and standard error were calculated from 2 experiments. Statistical analysis was performed  
848 with one-way ANOVA and asterisks indicate significant difference from DMSO. \*,  $p < 0.05$ ; \*\*,  
849  $p < 0.01$ . Rel.; relative.  
850

851 **Supplemental Figure 4:** Calu-3 cells were treated with 20  $\mu$ M Rap, Eve, Tem, Rid, or the  
852 equivalent volume of DMSO for 4 hours. HIV-CoV-2 (100 ng p24 equivalent) was added to cells  
853 and infection was measured by luciferase activity at 48 hours post-infection. Luciferase units  
854 were normalized to 100 in the DMSO condition. Means and standard error were calculated from  
855 3 experiments. Statistical analysis was performed with one-way ANOVA and asterisks indicate  
856 significant difference from DMSO. \*,  $p < 0.05$ ; \*\*,  $p < 0.01$ . Rel.; relative.  
857

858 **Supplemental Figure 5:** (A) HeLa-ACE2 cells were treated with 20  $\mu$ M Rap, Eve, Tem, Rid,  
859 Tac, or the equivalent volume of DMSO for 4 hours. Whole cell lysates were subjected to SDS-  
860 PAGE and Western blot analysis. Immunoblotting was performed with anti-IFITM2/3 and anti-  
861 actin on the same nitrocellulose membrane. (B) HeLa-ACE2 cells were treated with 20  $\mu$ M Rap,  
862 Eve, Tem, Rid, Tac, or the equivalent volume of DMSO for 4 hours. HIV-CoV-2 (100 ng p24  
863 equivalent) was added to cells and infection was measured by luciferase activity at 48 hours  
864 post-infection. Luciferase units were normalized to 100 in the DMSO condition. Means and  
865 standard error were calculated from 3 experiments. Statistical analysis was performed with one-  
866 way ANOVA and asterisks indicate significant difference from DMSO. \*,  $p < 0.05$ ; \*\*,  $p < 0.01$ .  
867 Rel.; relative. (C) HeLa-ACE2 were transfected with 0.5  $\mu$ g TFE $\Delta$ 30-GFP for 24 hours and

868 treated with 20  $\mu$ M Tem for four hours. Cells were then fixed, permeabilized, stained with anti-  
869 IFITM2/3, and imaged by confocal immunofluorescence microscopy. Representative images are  
870 shown and anti-IFITM2/3 staining in untreated HeLa-ACE2 are shown for comparison. (D)  
871 Whole cell lysates from HeLa WT and HeLa *TFEB* KO cells were subjected to SDS-PAGE and  
872 Western blot analysis. Immunoblotting was performed with anti-TFEB and anti-actin on the  
873 same nitrocellulose membrane.

874

875 **Supplemental Figure 6:** Body weight measurements for individual hamsters following  
876 injections with DMSO (A), Rap (B), or Rid (C) are plotted by day post-infection and presented  
877 as % body weight change relative to Day 0. Hamsters receiving one injection of 3 mg/kg DMSO,  
878 Rap, or Rid prior to infection (n=4, 1 injection) are indicated by black squares, while hamsters  
879 receiving one injection prior to infection as well as a second injection of 3 mg/kg DMSO, Rap,  
880 or Rid at Day 2 post-infection (n=4, 2 injections) are indicated by white squares. The average  
881 daily weight change for each group is indicated by grey and black lines, respectively. If and  
882 when a hamster lost 20% or more of its body weight, it was euthanized and body weight  
883 measurements were stopped.

884

## 885 **Acknowledgements**

886

887 We thank Michael Letko and Vincent Munster for providing VSV-luc/GFP seed particles  
888 and CoV and CoV-2 Spike plasmids, Thomas Gallagher for providing CoV, CoV-2, and MERS  
889 Spike plasmids, Alan Rein for facilitating lentiviral pseudovirus production, Scott H. Randell for  
890 providing UNCNN2TS, Ramnik J. Xavier for providing HeLa *TFEB* KO cells, and Eric O. Freed  
891 for providing primary HSAEC.

892

## 893 **Funding sources**

894

895 Work in the lab of AAC was funded by the Intramural Research Program, National  
896 Institutes of Health, National Cancer Institute, Center for Cancer Research and an Intramural  
897 Targeted Anti-COVID-19 award from the National Institute of Allergy and Infectious Diseases.  
898 Work in the lab of SMB was funded by the Division of Intramural Research, National Institutes  
899 of Health, National Institute of Allergy and Infectious Diseases. The content of this publication  
900 does not necessarily reflect the views or policies of the Department of Health and Human  
901 Services, nor does mention of trade names, commercial products, or organizations imply  
902 endorsement by the U.S. Government. Work in the lab of JSY was funded by National Institutes  
903 of Health grants AI130110, AI151230, AI142256, and HL154001.

904

## 905 **References**

906

- 907 1. Zhu, N., et al., *A Novel Coronavirus from Patients with Pneumonia in China, 2019*. New  
908 England Journal of Medicine, 2020. **382**(8): p. 727-733.
- 909 2. Wu, F., et al., *A new coronavirus associated with human respiratory disease in China*.  
910 Nature, 2020: p. 1-20.
- 911 3. Zhang, X., et al., *Viral and host factors related to the clinical outcome of COVID-19*.  
912 Nature, 2020: p. 1-18.

- 913 4. Aydillo, T., N.E. Babady, and M. Kamboj, *Shedding of Viable SARS-CoV-2 after*  
914 *Immunosuppressive Therapy for Cancer*. New England Journal of Medicine, 2020.  
915 **383**(26): p. 2586-2588.
- 916 5. Wei, J., et al., *SARS-CoV-2 infection in immunocompromised patients: humoral versus*  
917 *cell-mediated immunity*. Journal for immunotherapy of cancer, 2020. **8**(2): p. e000862.
- 918 6. Tarhini, H., et al., *Long term SARS-CoV-2 infectiousness among three*  
919 *immunocompromised patients: from prolonged viral shedding to SARS-CoV-2*  
920 *superinfection*. The Journal of Infectious Diseases, 2021.
- 921 7. Baang, J.H., et al., *Prolonged Severe Acute Respiratory Syndrome Coronavirus 2*  
922 *Replication in an Immunocompromised Patient*. The Journal of Infectious Diseases,  
923 2021. **223**(1): p. 23-27.
- 924 8. Avanzato, V.A., et al., *Case Study: Prolonged Infectious SARS-CoV-2 Shedding from an*  
925 *Asymptomatic Immunocompromised Individual with Cancer*. Cell, 2020. **183**(7): p. 1901-  
926 1912.e9.
- 927 9. Gordon, D.E., et al., *A SARS-CoV-2 protein interaction map reveals targets for drug*  
928 *repurposing*. Nature, 2020: p. 1-30.
- 929 10. Zhou, Y., et al., *Network-based drug repurposing for novel coronavirus 2019-*  
930 *nCoV/SARS-CoV-2*. Cell Discovery, 2020: p. 1-18.
- 931 11. Appelberg, S., et al., *Dysregulation in Akt/mTOR/HIF-1 signaling identified by proteo-*  
932 *transcriptomics of SARS-CoV-2 infected cells*. Emerging Microbes & Infections, 2020.  
933 **9**(1): p. 1748-1760.
- 934 12. Blagosklonny, M.V., *From causes of aging to death from COVID-19*. Aging, 2020.  
935 **12**(11): p. 10004-10021.
- 936 13. Ciliberto, G., R. Mancini, and M.G. Paggi, *Drug repurposing against COVID-19: focus*  
937 *on anticancer agents*. 2020: p. 1-9.
- 938 14. Husain, A. and S.N. Byrareddy, *Rapamycin as a potential repurpose drug candidate for*  
939 *the treatment of COVID-19*. Chemico-Biological Interactions, 2020. **331**: p. 109282.
- 940 15. Zheng, Y., R. Li, and S. Liu, *Immunoregulation with mTOR inhibitors to prevent*  
941 *COVID-19 severity: A novel intervention strategy beyond vaccines and specific antiviral*  
942 *medicines*. Journal of medical virology, 2020. **92**(9): p. 1495-1500.
- 943 16. Terrazzano, G., et al., *An Open Question: Is It Rational to Inhibit the mTor-Dependent*  
944 *Pathway as COVID-19 Therapy?* 2020: p. 1-5.
- 945 17. Ramaiah, M.J., *mTOR inhibition and p53 activation, microRNAs: The possible therapy*  
946 *against pandemic COVID-19*. Gene reports, 2020. **20**: p. 100765.
- 947 18. Zhavoronkov, A., *Geroprotective and senoremediative strategies to reduce the*  
948 *comorbidity, infection rates, severity, and lethality in gerophilic and gerolavic infections*.  
949 Aging, 2020. **12**(8): p. 6492-6510.
- 950 19. Willyard, C., *Ageing and Covid Vaccines*. Nature, 2020. **586**(7829): p. 352-354.
- 951 20. Omarjee, L., et al., *Targeting T-cell senescence and cytokine storm with rapamycin to*  
952 *prevent severe progression in COVID-19*. Clinical immunology (Orlando, Fla.), 2020.  
953 **216**: p. 108464.
- 954 21. Laplante, M. and D.M. Sabatini, *mTOR signaling in growth control and disease*. Cell,  
955 2012. **149**(2): p. 274-293.
- 956 22. Bertram, P.G., et al., *The 14-3-3 proteins positively regulate rapamycin-sensitive*  
957 *signaling*. Current biology : CB, 1998. **8**(23): p. 1259-1267.

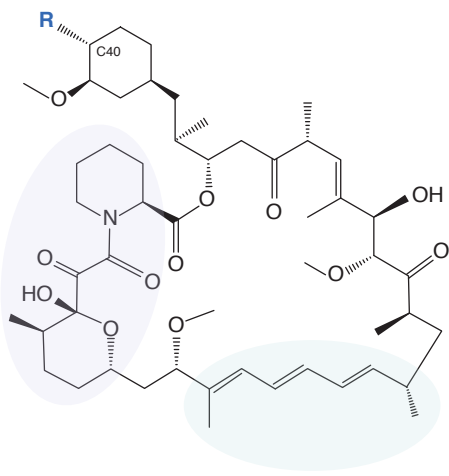
- 958 23. Vignot, S., et al., *mTOR-targeted therapy of cancer with rapamycin derivatives*. *Annals*  
959 *of Oncology*, 2005. **16**(4): p. 525-537.
- 960 24. Lamming, D.W., et al., *Rapalogs and mTOR inhibitors as anti-aging therapeutics*.  
961 *Journal of Clinical Investigation*, 2013. **123**(3): p. 980-989.
- 962 25. Abdel-Magid, A.F., *Rapalogs Potential as Practical Alternatives to Rapamycin*. *ACS*  
963 *medicinal chemistry letters*, 2019. **10**(6): p. 843-845.
- 964 26. Benjamin, D., et al., *Rapamycin passes the torch: a new generation of mTOR inhibitors*.  
965 *Nature Reviews Drug Discovery*, 2011: p. 1-13.
- 966 27. Marz, A.M., et al., *Large FK506-Binding Proteins Shape the Pharmacology of*  
967 *Rapamycin*. *Molecular and Cellular Biology*, 2013. **33**(7): p. 1357-1367.
- 968 28. Zoncu, R., A. Efeyan, and D.M. Sabatini, *mTOR: from growth signal integration to*  
969 *cancer, diabetes and ageing*. *Nature Reviews in Molecular Cell Biology*, 2011. **12**(1): p.  
970 21-35.
- 971 29. Chi, H., *Regulation and function of mTOR signalling in T cell fate decisions*. *Nature*  
972 *Reviews Immunology*, 2012: p. 1-14.
- 973 30. Mangalmurti, N. and C.A. Hunter, *Cytokine Storms: Understanding COVID-19*.  
974 *Immunity*, 2020. **53**(1): p. 19-25.
- 975 31. Mehta, P., et al., *COVID-19: consider cytokine storm syndromes and*  
976 *immunosuppression*. *Lancet (London, England)*, 2020. **395**(10229): p. 1033-1034.
- 977 32. Manjili, R.H., et al., *COVID-19 as an Acute Inflammatory Disease*. *The Journal of*  
978 *Immunology*, 2020. **205**(1): p. 12-19.
- 979 33. Bischof, E., et al., *The potential of rapalogs to enhance resilience against SARS-CoV-2*  
980 *infection and reduce the severity of COVID-19*. *The Lancet. Healthy longevity*, 2021.  
981 **2**(2): p. e105-e111.
- 982 34. Mullen, P.J., et al., *SARS-CoV-2 infection rewires host cell metabolism and is potentially*  
983 *susceptible to mTORC1 inhibition*. *Nature communications*, 2021: p. 1-10.
- 984 35. Alsuwaidi, A.R., et al., *Sirolimus alters lung pathology and viral load following influenza*  
985 *A virus infection*. *Respiratory research*, 2017. **18**(1): p. 136.
- 986 36. Huang, C.-T., et al., *Rapamycin adjuvant and exacerbation of severe influenza in an*  
987 *experimental mouse model*. *Scientific Reports*, 2017. **7**(1): p. 873-8.
- 988 37. Shi, G., et al., *mTOR inhibitors lower an intrinsic barrier to virus infection mediated by*  
989 *IFITM3*. *Proceedings of the National Academy of Sciences of the United States of*  
990 *America*, 2018. **115**(43): p. E10069-E10078.
- 991 38. Ozog, S., et al., *Resveratrol trimer enhances gene delivery to hematopoietic stem cells by*  
992 *reducing antiviral restriction at endosomes*. *Blood*, 2019. **134**(16): p. 1298-1311.
- 993 39. Shi, G., O. Schwartz, and A.A. Compton, *More than meets the I: the diverse antiviral*  
994 *and cellular functions of interferon-induced transmembrane proteins*. *Retrovirology*,  
995 2017. **14**(1): p. 1-11.
- 996 40. Majdoul, S. and A.A. Compton, *Lessons in self-defence: inhibition of virus entry by*  
997 *intrinsic immunity*. *Nature Reviews Immunology*, 2021.
- 998 41. Bestle, D., et al., *TMPRSS2 and furin are both essential for proteolytic activation of*  
999 *SARS-CoV-2 in human airway cells*. *Life science alliance*, 2020. **3**(9): p. e202000786.
- 1000 42. Hoffmann, M., H. Kleine-Weber, and S. Pöhlmann, *A Multibasic Cleavage Site in the*  
1001 *Spike Protein of SARS-CoV-2 Is Essential for Infection of Human Lung Cells*. *Molecular*  
1002 *Cell*, 2020. **78**(4): p. 779-784.e5.

- 1003 43. Hoffmann, M., et al., *SARS-CoV-2 Cell Entry Depends on ACE2 and TMPRSS2 and Is*  
1004 *Blocked by a Clinically Proven Protease Inhibitor*. Cell, 2020: p. 1-19.
- 1005 44. Shi, G., et al., *mTOR inhibitors lower an intrinsic barrier to virus infection mediated by*  
1006 *IFITM3*. Proceedings of the National Academy of Sciences of the United States of  
1007 America, 2018. **115**(43): p. E10069-E10078.
- 1008 45. Mejlvang, J., et al., *Starvation induces rapid degradation of selective autophagy*  
1009 *receptors by endosomal microautophagy*. J Cell Biol, 2018. **217**(10): p. 3640-3655.
- 1010 46. Olsvik, H.L., et al., *Endosomal microautophagy is an integrated part of the autophagic*  
1011 *response to amino acid starvation*. Autophagy, 2019. **15**(1): p. 182-183.
- 1012 47. Sahu, R., et al., *Microautophagy of cytosolic proteins by late endosomes*. Dev Cell, 2011.  
1013 **20**(1): p. 131-9.
- 1014 48. Bozzo, C.P., et al., *IFITM proteins promote SARS-CoV-2 infection of human lung cells*.  
1015 bioRxiv, 2020. **1**: p. 261-47.
- 1016 49. Kolos, J.M., et al., *FKBP Ligands-Where We Are and Where to Go?* Frontiers in  
1017 pharmacology, 2018. **9**: p. 1425.
- 1018 50. Roczniak-Ferguson, A., et al., *The transcription factor TFEB links mTORC1 signaling to*  
1019 *transcriptional control of lysosome homeostasis*. Science signaling, 2012. **5**(228): p. ra42.
- 1020 51. Martina, J.A., et al., *MTORC1 functions as a transcriptional regulator of autophagy by*  
1021 *preventing nuclear transport of TFEB*. Autophagy, 2012. **8**(6): p. 903-14.
- 1022 52. Settembre, C., et al., *A lysosome-to-nucleus signalling mechanism senses and regulates*  
1023 *the lysosome via mTOR and TFEB*. The EMBO journal, 2012. **31**(5): p. 1095-1108.
- 1024 53. Zhang, X., et al., *Rapamycin directly activates lysosomal mucolipin TRP channels*  
1025 *independent of mTOR*. PLoS Biology, 2019. **17**(5): p. e3000252-24.
- 1026 54. Alsuwaidi, A.R., et al., *Sirolimus alters lung pathology and viral load following influenza*  
1027 *A virus infection*. Respiratory research, 2017. **18**(1): p. 1-8.
- 1028 55. Tostanoski, L.H., et al., *Ad26 vaccine protects against SARS-CoV-2 severe clinical*  
1029 *disease in hamsters*. Nat Med, 2020. **26**(11): p. 1694-1700.
- 1030 56. Sasongko, T.H., et al., *Rapamycin and its analogues (rapalogs) for Tuberous Sclerosis*  
1031 *Complex-associated tumors: a systematic review on non-randomized studies using meta-*  
1032 *analysis*. Orphanet Journal of Rare Diseases, 2015: p. 1-11.
- 1033 57. Reagan-Shaw, S., M. Nihal, and N. Ahmad, *Dose translation from animal to human*  
1034 *studies revisited*. FASEB J, 2008. **22**(3): p. 659-61.
- 1035 58. Cloughesy, T.F., et al., *Antitumor activity of rapamycin in a Phase I trial for patients*  
1036 *with recurrent PTEN-deficient glioblastoma*. PLoS Med, 2008. **5**(1): p. e8.
- 1037 59. Sun, Y., et al., *Phase II study of the safety and efficacy of temsirolimus in East Asian*  
1038 *patients with advanced renal cell carcinoma*. Jpn J Clin Oncol, 2012. **42**(9): p. 836-44.
- 1039 60. Martynov, M.Y., V.A. Kutashov, and O.V. Ulyanova, *COVID 19 in a family with rare*  
1040 *genetic disease of the nervous system*. Neurology, Neuropsychiatry, Psychosomatics,  
1041 2022. **14**(1): p. 108-114.
- 1042 61. Medina, D.L., et al., *Lysosomal calcium signalling regulates autophagy through*  
1043 *calcineurin and TFEB*. Nature Cell Biology, 2015. **17**(3): p. 288-299.
- 1044 62. Schuck, S., *Microautophagy - distinct molecular mechanisms handle cargoes of many*  
1045 *sizes*. Journal of Cell Science, 2020. **133**(17).
- 1046 63. Oku, M. and Y. Sakai, *Three Distinct Types of Microautophagy Based on Membrane*  
1047 *Dynamics and Molecular Machineries*. BioEssays, 2018. **40**(6): p. 1800008-6.

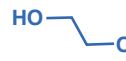
- 1048 64. Santambrogio, L. and A.M. Cuervo, *Chasing the elusive mammalian microautophagy*.  
1049 *Autophagy*, 2011. **7**(6): p. 652-4.
- 1050 65. Tekirdag, K. and A.M. Cuervo, *Chaperone-mediated autophagy and endosomal*  
1051 *microautophagy: Jointed by a chaperone*. *Journal of Biological Chemistry*, 2018.  
1052 **293**(15): p. 5414-5424.
- 1053 66. Mijaljica, D., M. Prescott, and R.J. Devenish, *Microautophagy in mammalian cells:*  
1054 *revisiting a 40-year-old conundrum*. *Autophagy*, 2011. **7**(7): p. 673-682.
- 1055 67. Sato, M., et al., *Rapamycin activates mammalian microautophagy*. *Journal of*  
1056 *Pharmacological Science*, 2019. **140**(2): p. 201-204.
- 1057 68. Yang, X., et al., *TORC1 regulates vacuole membrane composition through ubiquitin- and*  
1058 *ESCRT-dependent microautophagy*. *The Journal of Cell Biology*, 2020. **219**(3).
- 1059 69. Li, M., et al., *Ubiquitin-Dependent Lysosomal Membrane Protein Sorting and*  
1060 *Degradation*. *Molecular Cell*, 2015. **57**(3): p. 467-478.
- 1061 70. Chesarino, N.M., T.M. McMichael, and J.S. Yount, *E3 Ubiquitin Ligase NEDD4*  
1062 *Promotes Influenza Virus Infection by Decreasing Levels of the Antiviral Protein*  
1063 *IFITM3*. *PLoS Pathogens*, 2015. **11**(8): p. e1005095.
- 1064 71. Compton, A.A., et al., *Natural mutations in IFITM3 modulate post-translational*  
1065 *regulation and toggle antiviral specificity*. *EMBO reports*, 2016. **17**(11): p. 1657-1671.
- 1066 72. Yang, X., et al., *TORC1 regulates vacuole membrane composition through ubiquitin- and*  
1067 *ESCRT-dependent microautophagy*. 2019. **8**: p. 1835-53.
- 1068 73. Di Fruscio, G., et al., *Lysoplex: An efficient toolkit to detect DNA sequence variations in*  
1069 *the autophagy-lysosomal pathway*. *Autophagy*, 2015. **11**(6): p. 928-38.
- 1070 74. Zhao, X., et al., *Interferon induction of IFITM proteins promotes infection by human*  
1071 *coronavirus OC43*. *Proceedings of the National Academy of Sciences*, 2014. **111**(18): p.  
1072 6756-6761.
- 1073 75. Shi, G., et al., *Opposing activities of IFITM proteins in SARS-CoV-2 infection*. *The*  
1074 *EMBO journal*, 2020. **3**: p. e201900542-12.
- 1075 76. Winstone, H., et al., *The polybasic cleavage site in the SARS-CoV-2 spike modulates viral*  
1076 *sensitivity to Type I interferon and IFITM2*. *Journal of Virology*, 2021.
- 1077 77. Zhao, X., et al., *LY6E Restricts Entry of Human Coronaviruses, Including Currently*  
1078 *Pandemic SARS-CoV-2*. *Journal of Virology*, 2020. **94**(18).
- 1079 78. Zang, R., et al., *Cholesterol 25-hydroxylase suppresses SARS-CoV-2 replication by*  
1080 *blocking membrane fusion*. *Proceedings of the National Academy of Sciences of the*  
1081 *United States of America*, 2020. **32**: p. 202012197.
- 1082 79. Huang, I.C., et al., *Distinct patterns of IFITM-mediated restriction of filoviruses, SARS*  
1083 *coronavirus, and influenza A virus*. *PLoS Pathogens*, 2011. **7**(1): p. e1001258.
- 1084 80. Zhao, X., et al., *Identification of Residues Controlling Restriction versus Enhancing*  
1085 *Activities of IFITM Proteins on Entry of Human Coronaviruses*. *Journal of Virology*,  
1086 2018. **92**(6): p. 374-17.
- 1087 81. Zani, A., et al., *Interferon-induced transmembrane protein 3 (IFITM3) limits lethality of*  
1088 *SARS-CoV-2 in mice*. *bioRxiv*, 2021.
- 1089 82. Beyer, D.K. and A. Forero, *Mechanisms of Antiviral Immune Evasion of SARS-CoV-2*. *J*  
1090 *Mol Biol*, 2021: p. 167265.
- 1091 83. Hachim, M.Y., et al., *Interferon-Induced Transmembrane Protein (IFITM3) Is*  
1092 *Upregulated Explicitly in SARS-CoV-2 Infected Lung Epithelial Cells*. *Frontiers in*  
1093 *Immunology*, 2020. **11**: p. 1372.



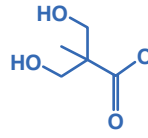
- 1094 84. Blanco-Melo, D., et al., *Imbalanced Host Response to SARS-CoV-2 Drives Development*  
1095 *of COVID-19*. Cell, 2020. **181**(5): p. 1036-1045.e9.
- 1096 85. Ziegler, C.G.K., et al., *Impaired local intrinsic immunity to SARS-CoV-2 infection in*  
1097 *severe COVID-19*. bioRxiv, 2021: p. 2021.02.20.431155.
- 1098 86. Zhang, Y., et al., *Interferon-induced transmembrane protein-3 genetic variant rs12252-*  
1099 *C is associated with disease severity in COVID-19*. The Journal of Infectious Diseases,  
1100 2020.
- 1101 87. Nikoloudis, D., D. Kountouras, and A. Hiona, *The frequency of combined IFITM3*  
1102 *haplotype involving the reference alleles of both rs12252 and rs34481144 is in line with*  
1103 *COVID-19 standardized mortality ratio of ethnic groups in England*. PeerJ, 2020. **8**: p.  
1104 e10402.
- 1105 88. Carey, K.L., et al., *TFEB Transcriptional Responses Reveal Negative Feedback by*  
1106 *BHLHE40 and BHLHE41*. Cell Rep, 2020. **33**(6): p. 108371.
- 1107 89. Leist, S.R., et al., *A Mouse-Adapted SARS-CoV-2 Induces Acute Lung Injury and*  
1108 *Mortality in Standard Laboratory Mice*. Cell, 2020. **183**(4): p. 1070-1085 e12.
- 1109 90. Chiramel, A.I., et al., *TRIM5 $\alpha$  Restricts Flavivirus Replication by Targeting the Viral*  
1110 *Protease for Proteasomal Degradation*. CellReports, 2019. **27**(11): p. 3269-3283.e6.
- 1111 91. Letko, M., A. Marzi, and V. Munster, *Functional assessment of cell entry and receptor*  
1112 *usage for SARS-CoV-2 and other lineage B betacoronaviruses*. Nature Microbiology,  
1113 2020. **11**: p. 1-17.
- 1114 92. Compton, A.A., et al., *IFITM Proteins Incorporated into HIV-1 Virions Impair Viral*  
1115 *Fusion and Spread*. Cell Host & Microbe, 2014. **16**(6): p. 736-747.
- 1116



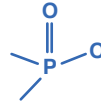
HO Sirolimus (Rapamycin)



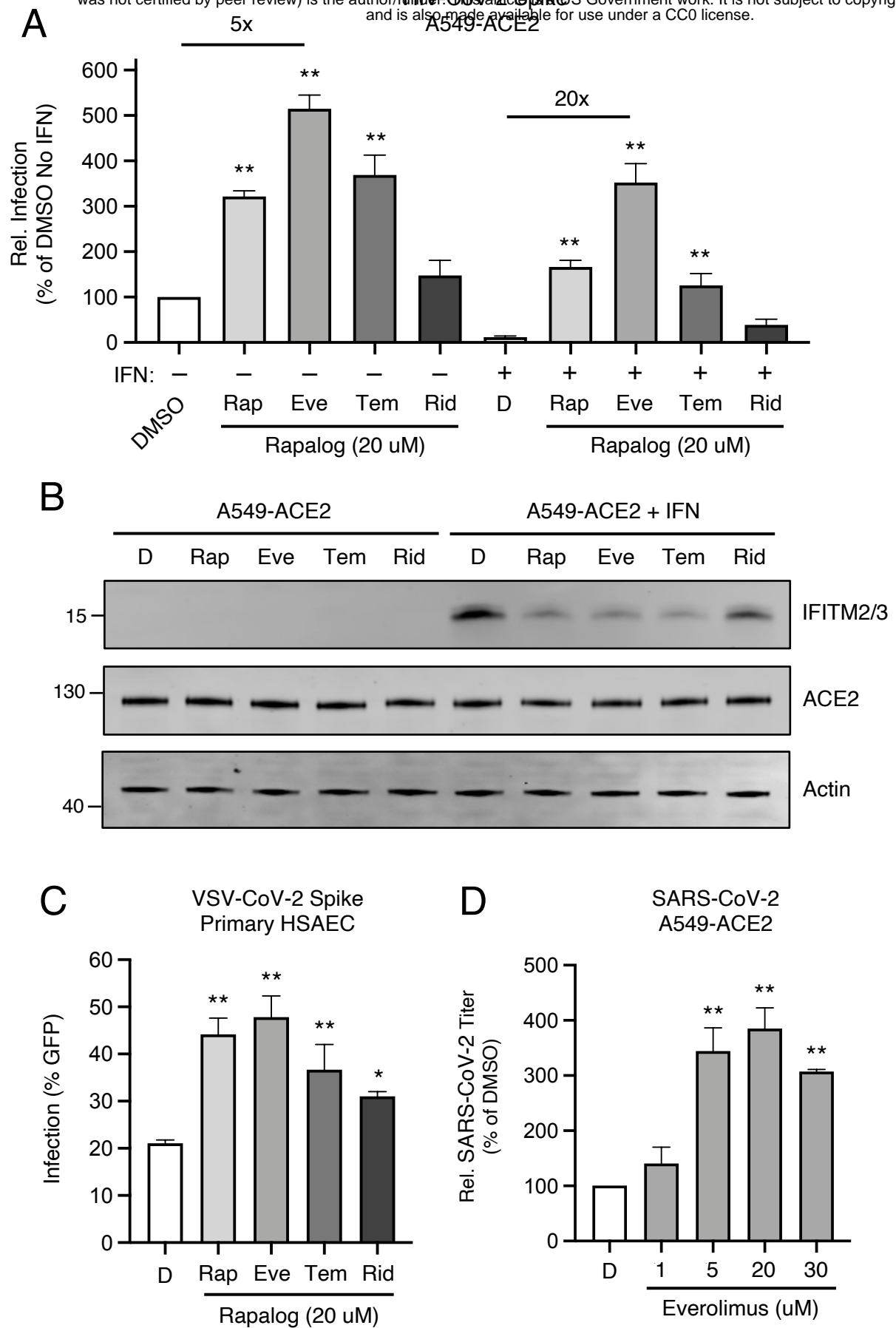
Everolimus

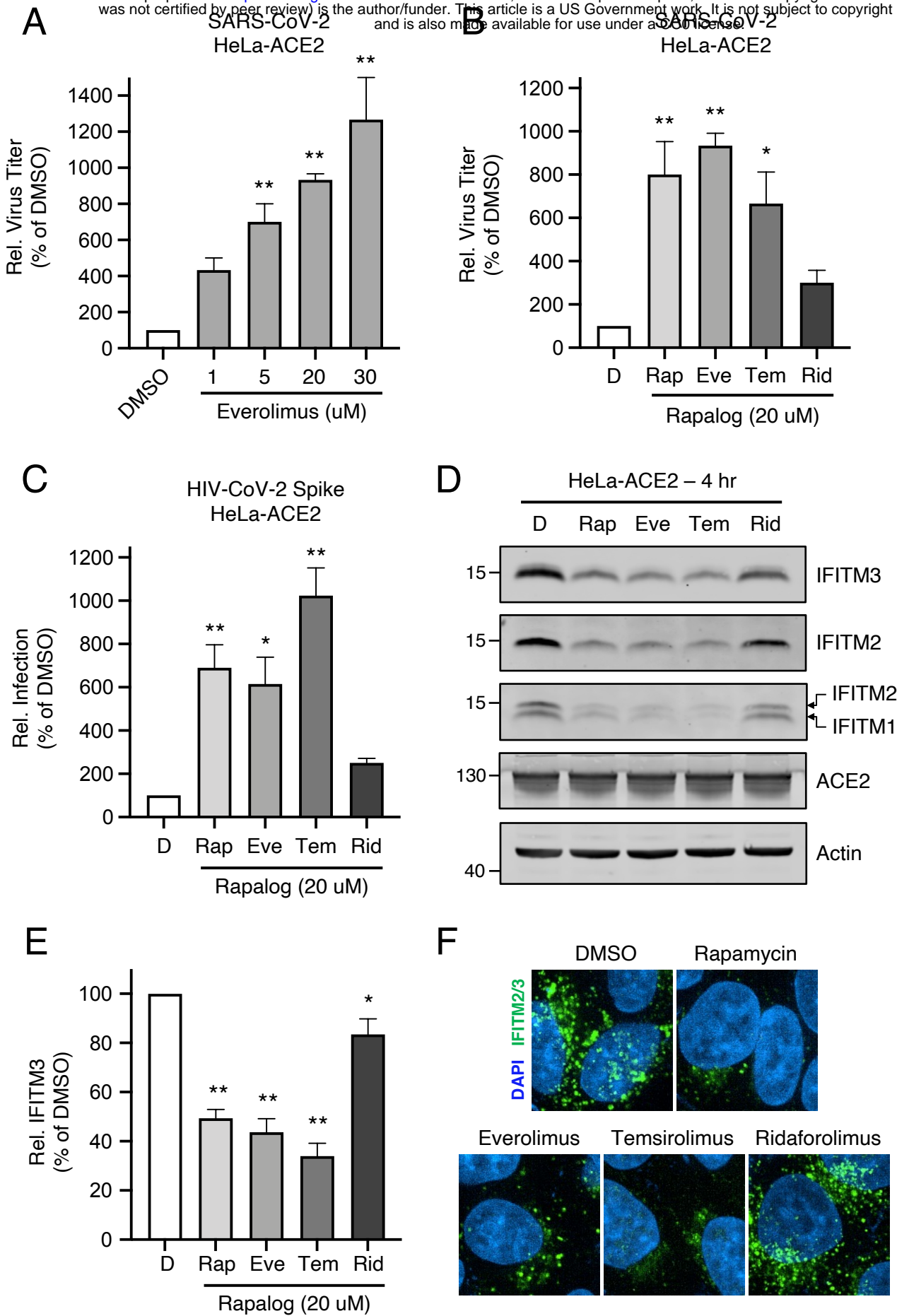


Temsirolimus

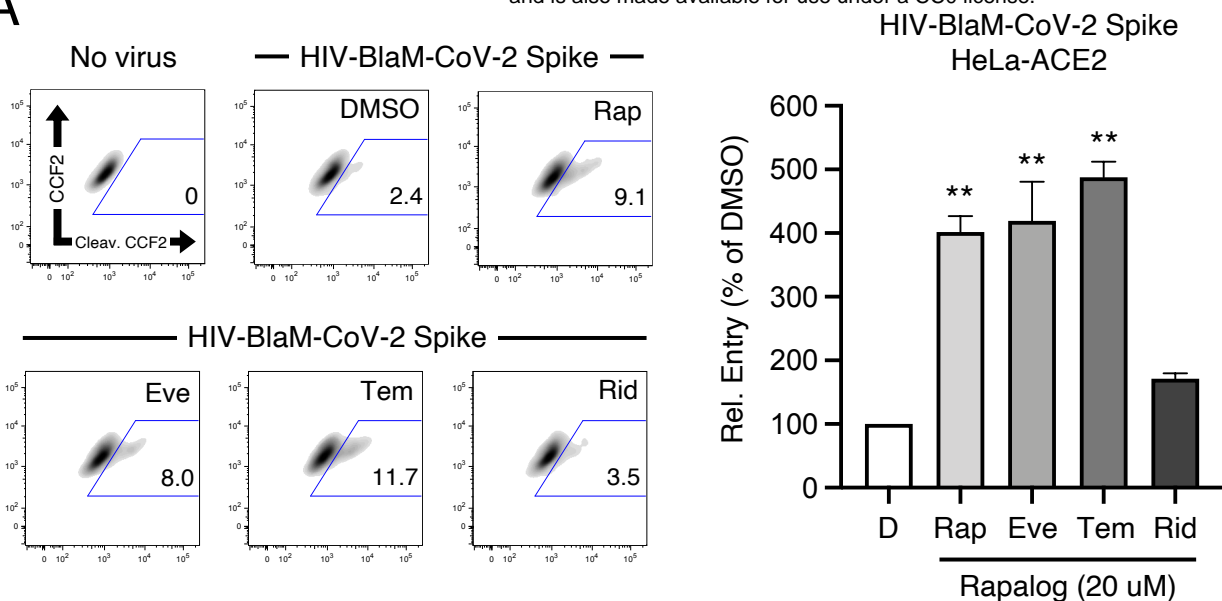


Ridaforolimus

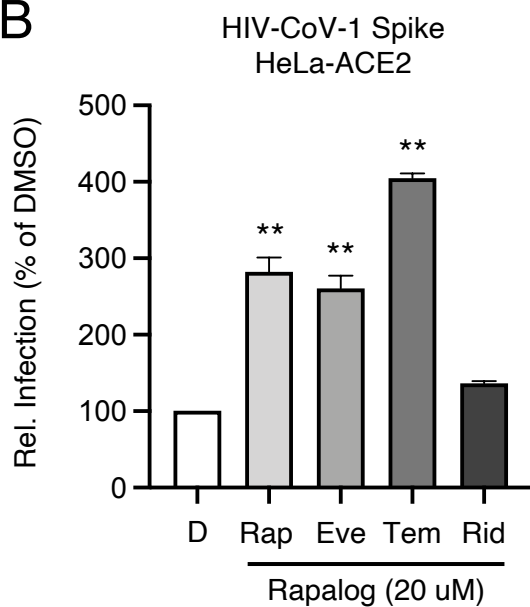




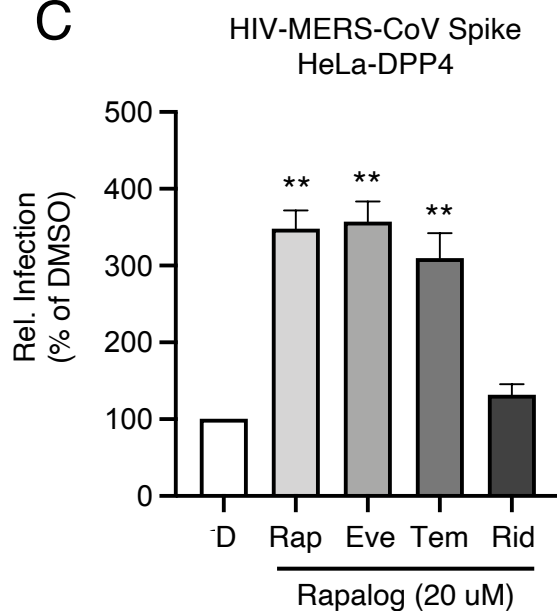
**A**



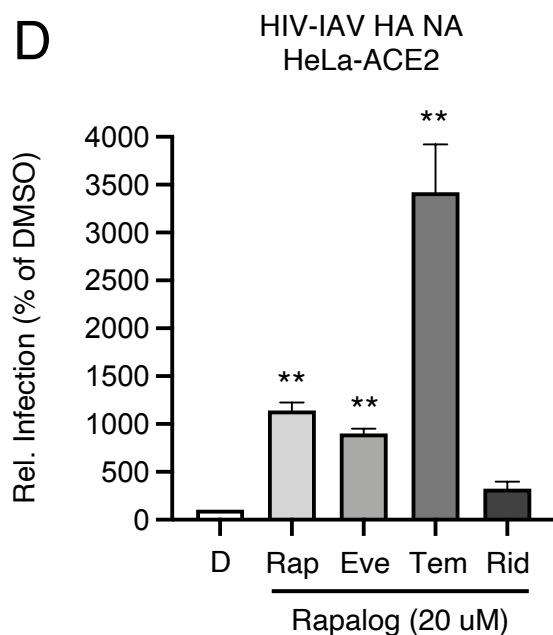
**B**



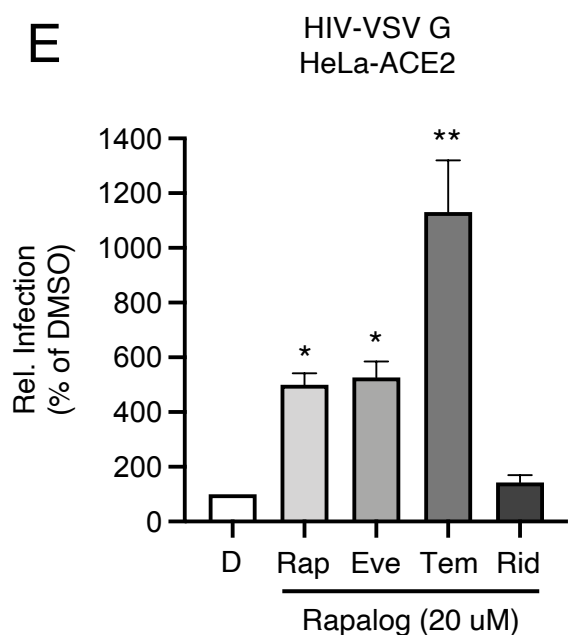
**C**

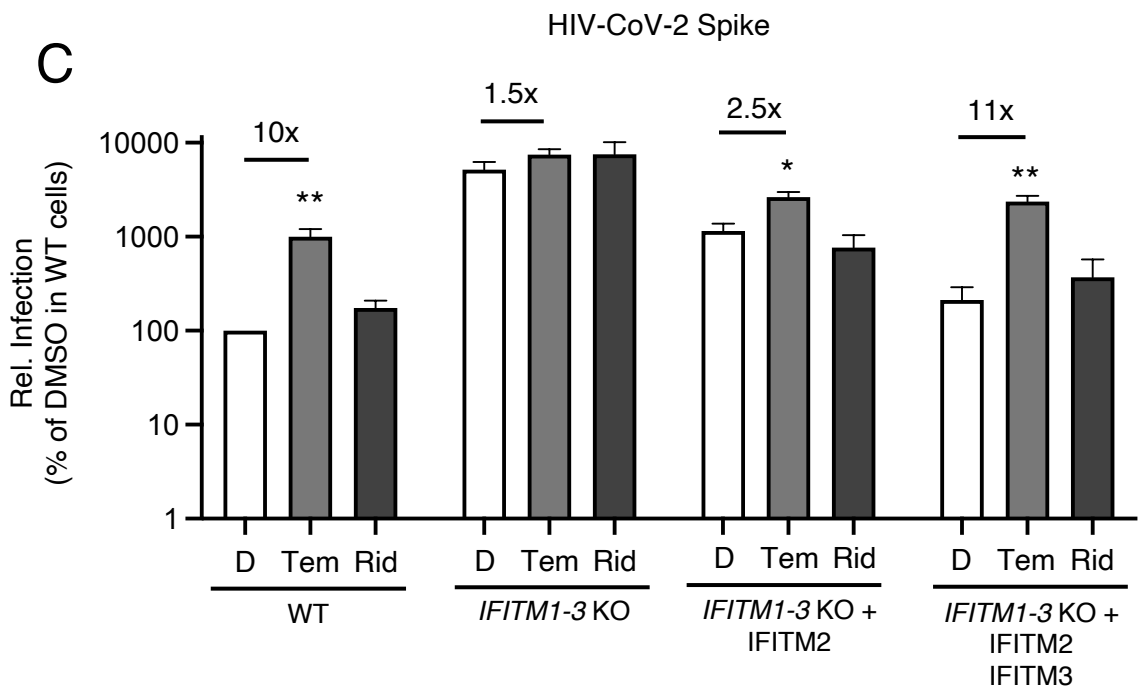
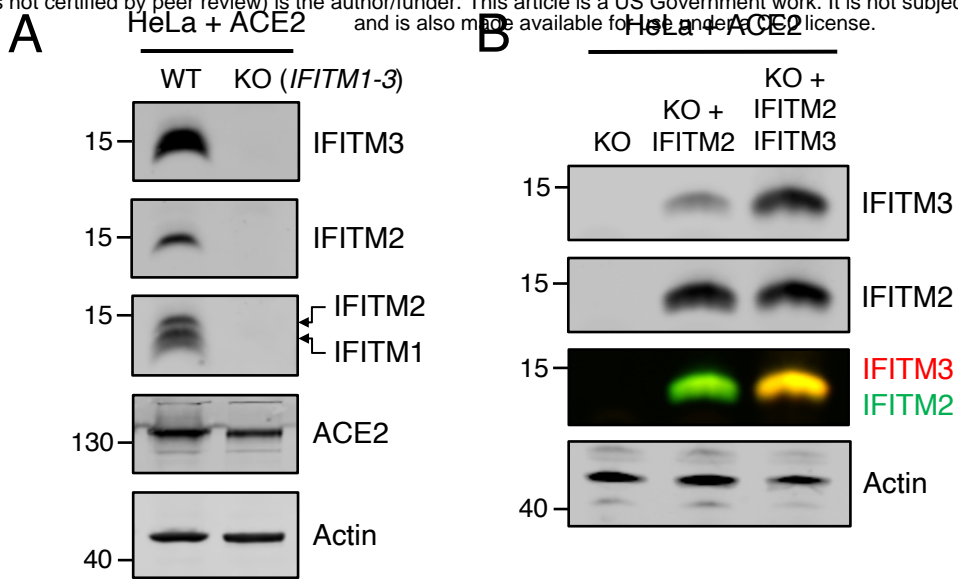


**D**

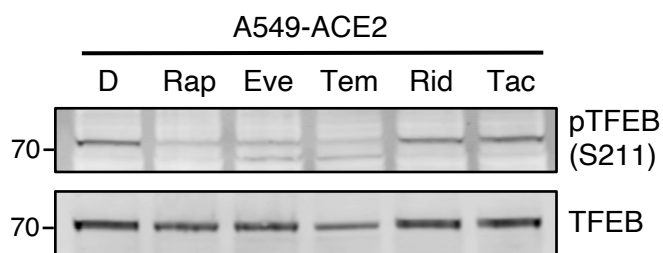


**E**

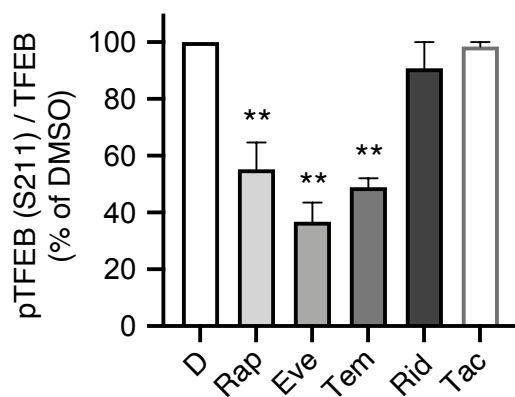




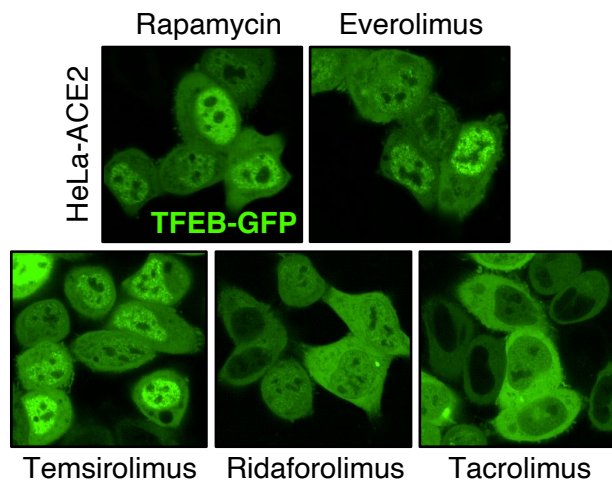
**A**



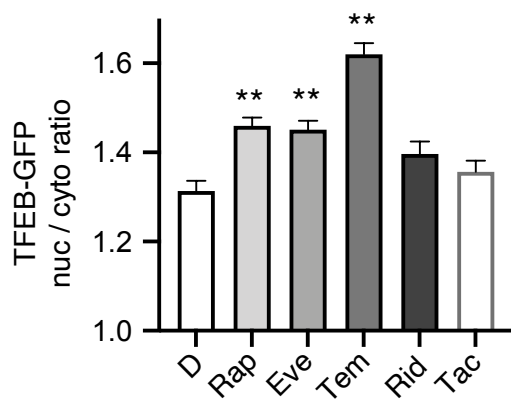
**B**



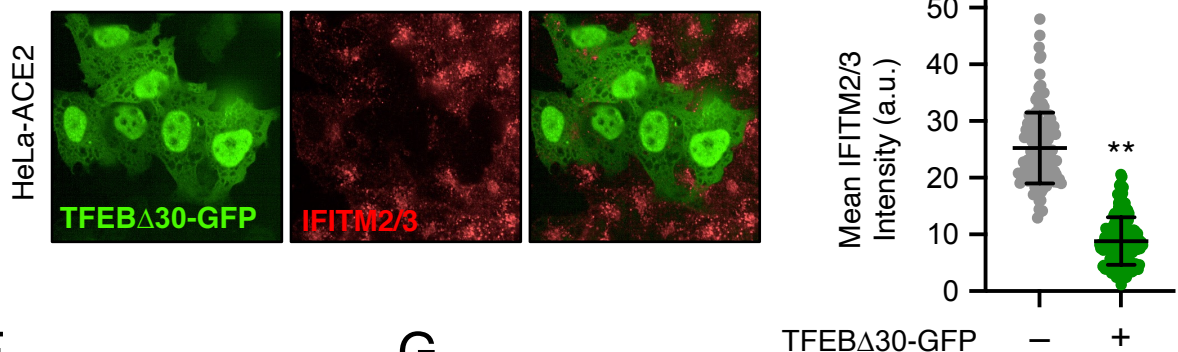
**C**



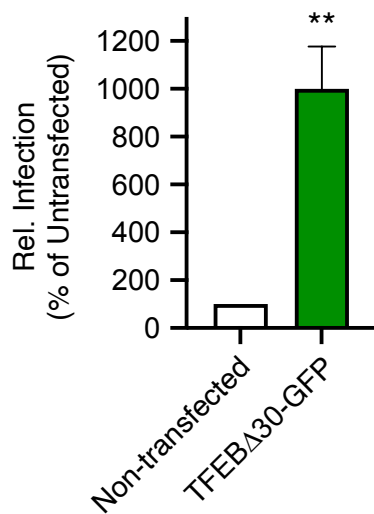
**D**



**E**



**F**



**G**

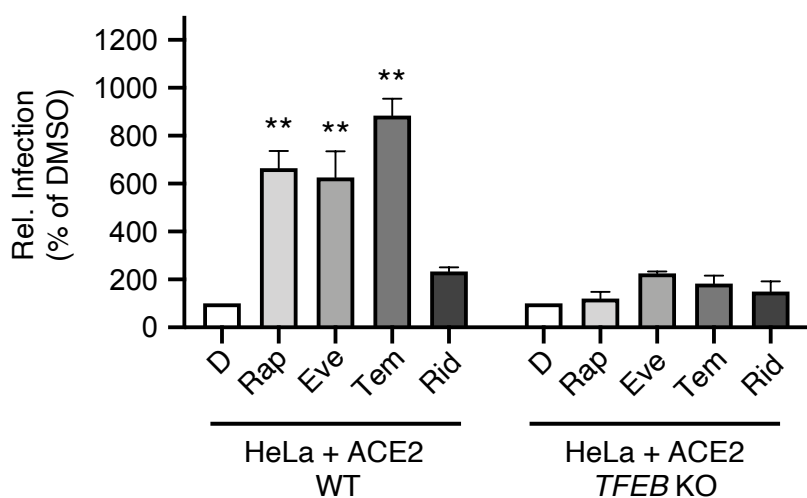


Figure 7

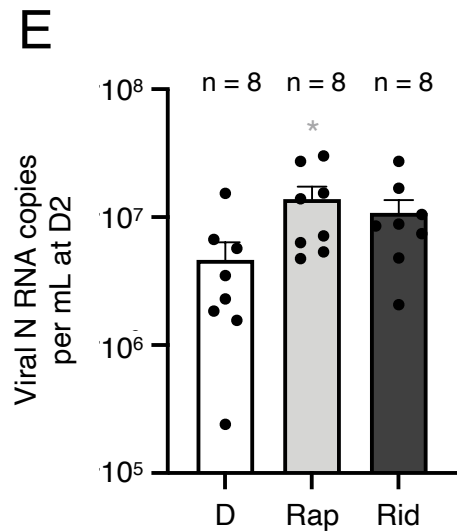
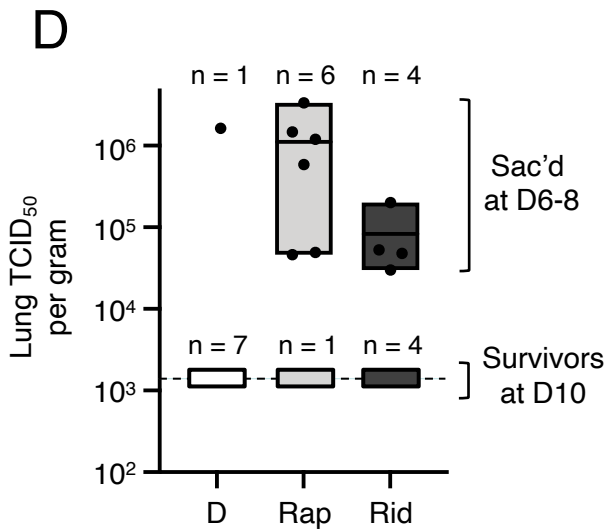
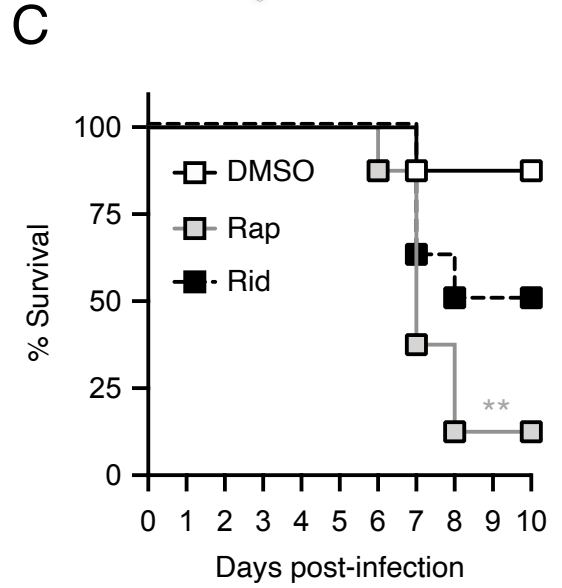
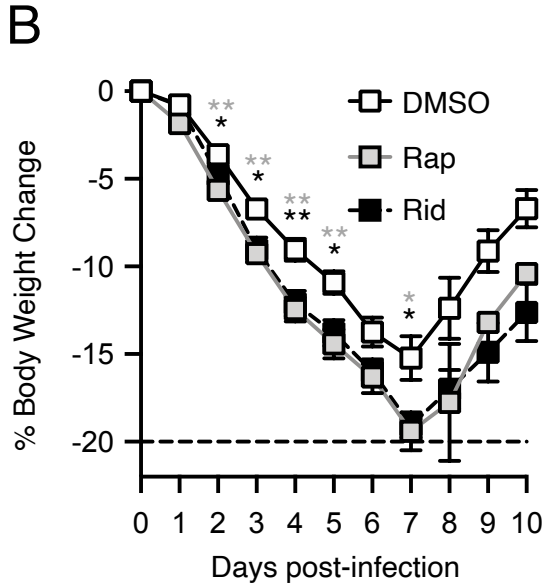
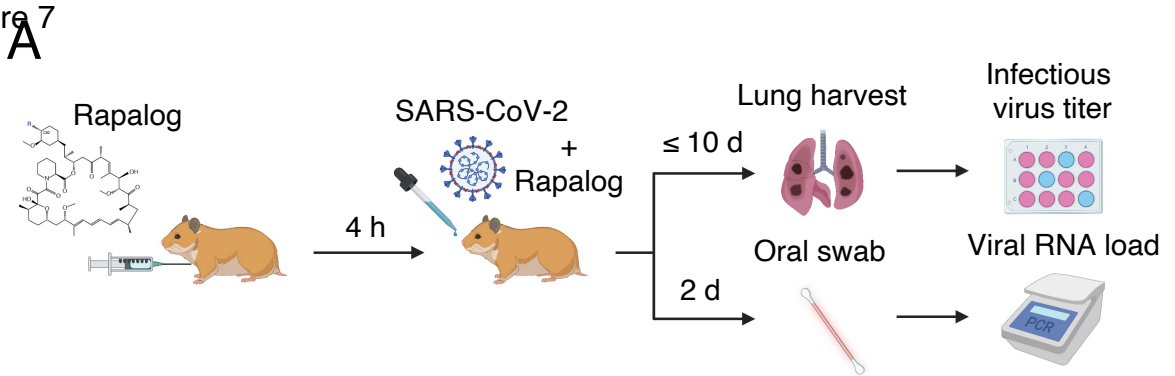
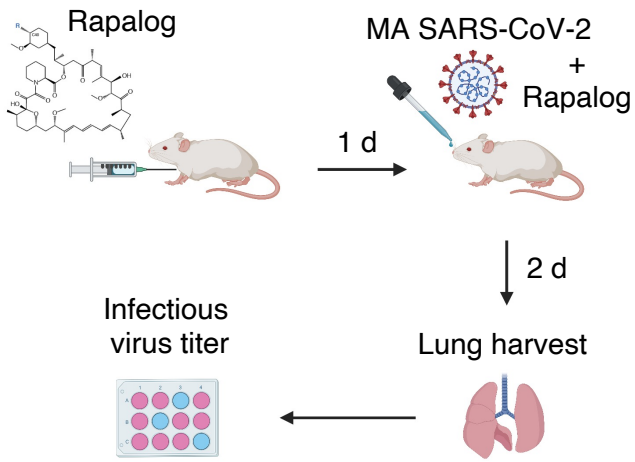


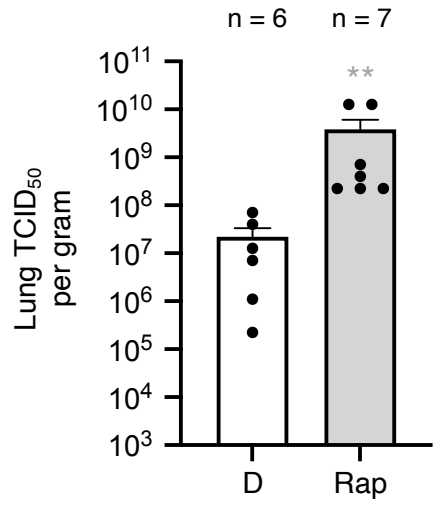


Figure 8

A



B



C

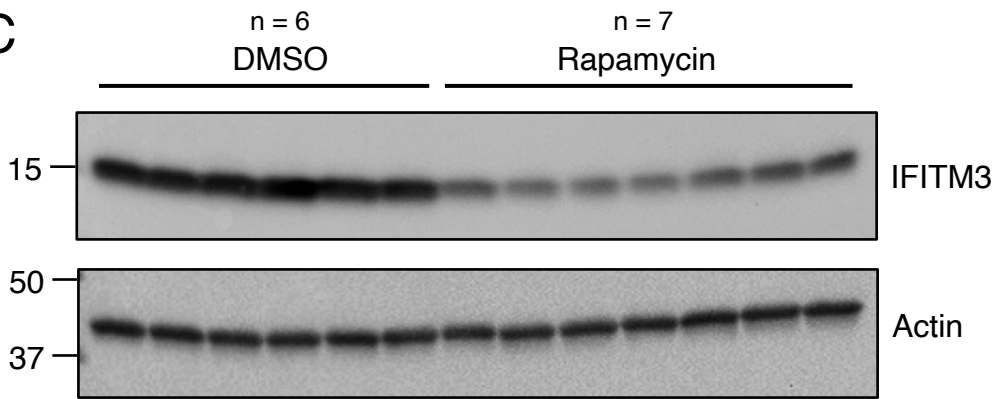


Figure 9

NUCLEUS

